Modeling neutral beam injection in Tokamaks

BY YOUJUN HU

Institute of plasma physics, Chinese Academy of Sciences
Email: yjhu@ipp.cas.cn

Abstract

A numerical code modeling the deposition and collisional transport of neutral beam particles in tokamaks is being developed. These notes discusses the physical models used in the code.

1 Neutral beam source

To create beam of neutral particles of high energy for the purpose of heating tokamak plasma, one usually needs a system consisting of (1) an ion source, which produces low-energy ions, (2) a set of accelerating electrodes, which is attached to the window of the ion-source arc chamber, to accelerate the ions to high-energy, (3) a neutralizing chamber, which neutralizes the high-energy ions, and (4) a bending magnet to remove remained charged particles from the beam.

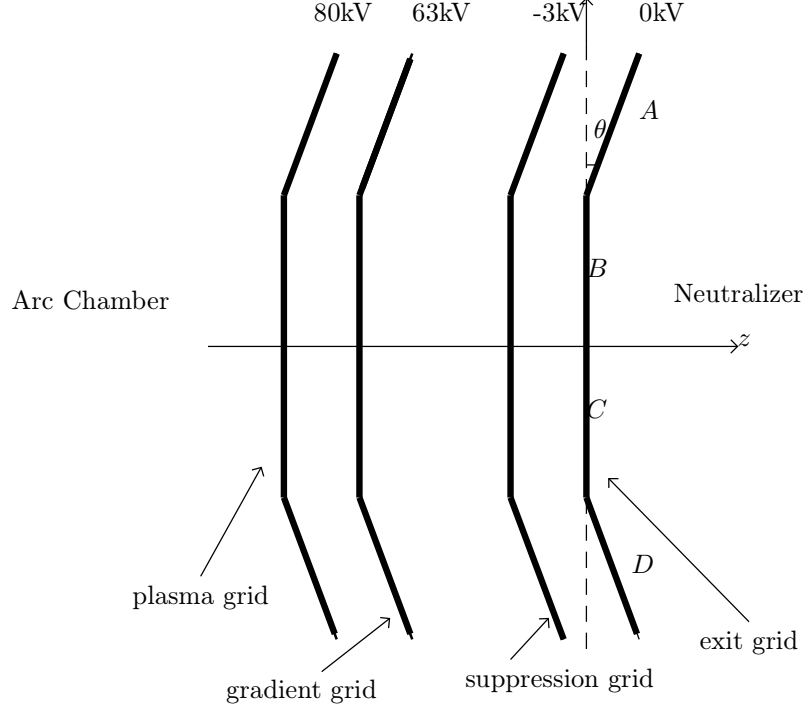An example of the accelerating electrodes on EAST neutral beam system is shown in Fig. 1.

Figure 1. Four groups of accelerating electrode grids of the ion source of EAST neutral beam injector, which are called plasma grid, gradient grid, suppression grid, and exit grid, respectively. Every electrode grid has four sub-electrode, indicated by A, B, C, and D on the figure. Sub-electrodes A and D are rotated to the right with respect to the centeral sub-electordes B and C by a small angle $\theta = \left(1\frac{1}{12}\right)$ degree. This angle is exaggerated on the figure. A typical setting of the voltage on the grids is indicated on the figure.

The exit grid on ion source of EAST NBI is rectangular with horizontal width being 0.12m (changed to 0.1m, from XieYaHong, 2025) and vertical hight 0.48m.

1.1 Beam focus

The central beam from each of the four sub-electrodes is perpendicular to the corresponding grid plane. As is shown in Fig. 1, two of the sub-electrodes A and D are tilted to the right with respect to the centeral sub-electordes by a small

angle θ. This focuses the central beams from A and D with a focal length given by

$$f_b \approx \frac{2y_0}{\tan(2\theta/3)}, \tag{1}$$

where y_0 is the vertical half-width of the sub-electrode, as shown in Fig. 2. [Proof of Eq. (1): Using the geometry given in Fig. 2, we have $\alpha_1 + \alpha_2 = \theta$ and $\sin\alpha_1 = 2\sin\alpha_2$. Since θ is small, both α_1 and α_2 are small. Thus we have the approximation $\sin\alpha_1 \approx \alpha_1$ and $\sin\alpha_2 = \alpha_2$. Using these, we obtain $\alpha_1 = 2\theta/3$. The focal length is then written as $f_b = 2y_0/\tan(\alpha_1) = 2y_0/\tan(2\theta/3)$.] For $\theta = \left(1\frac{1}{12}\right)$degree and $y_0 = 0.06m$, Eq. (1) gives $f_b = 9.5194m$.
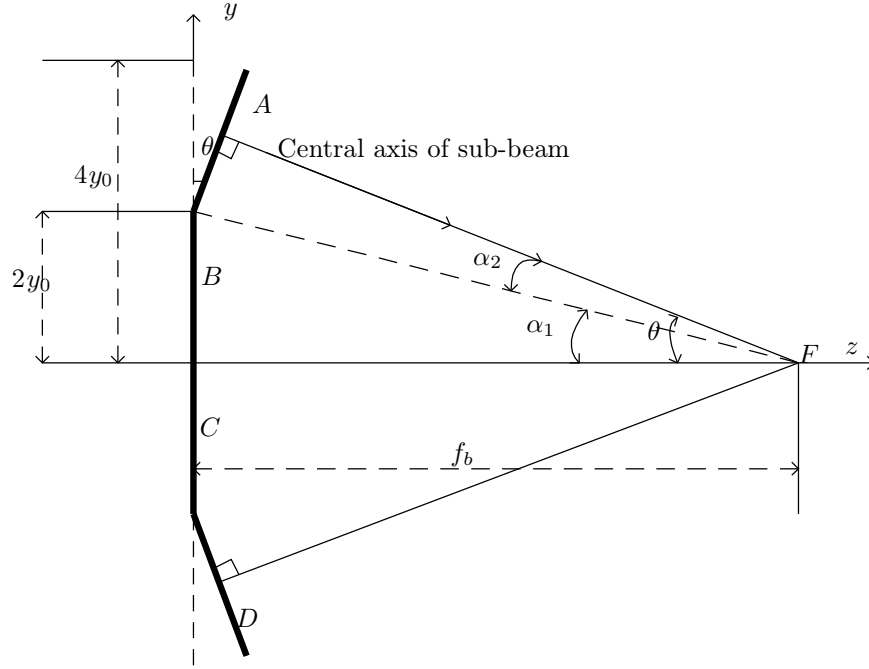

Figure 2. Geometry of exit electrode of the ion source of EAST neutral beam injector. The electrode has four sub-electrodes, indicated by A, B, C, and D on the figure. The vertical width of each sub-electrode is $2y_0$ with $y_0 = 0.06m$. Sub-electrodes A and D are rotated to the right with respect to the centeral sub-electordes B and C by a small angle $\theta = \left(1\frac{1}{12}\right)$degree. The central axis of the two sub-beams (beams from electrode A and D) intersect at F. The vertical focal length f_b is defined as the distance from point F to the electrode BC plane.

The above focal length is for the vertical plane. Similar defintion can be made for the horizontal focal length. The horizontal focal length is infinity for EAST

NBI because all the sub-electrodes are flat in the horizontal direction

1.2 Beam divergence

The direction of velocity of ions emerging from the exit grid of the ion-source can deviate from the central axis of the beam. This deviation is called beam divergence. Fig. 3 shows the beam divergence in the yz plane.
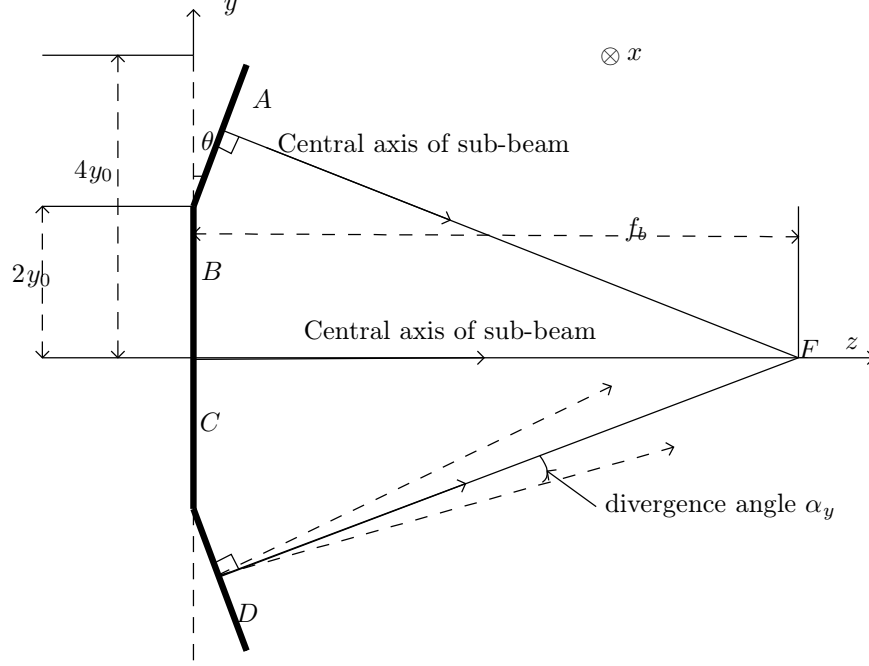

Figure 3. The included angle between the projection of central axis of the beam in yz plane and the projection of the particle velocity in yz plane is denoted by α_{yz}. Similar definition can be made for α_{xz}.

Assume that the deviation of particle velcoity direction from the central beam direction satisfies the following Gaussian distribution:

$$P(\alpha_{yz}) = \frac{1}{\sqrt{2\pi}\alpha_{yz0}}\exp\left(-\frac{\alpha_{yz}^2}{2\alpha_{yz0}^2}\right), \tag{2}$$

and

$$P(\alpha_{xz}) = \frac{1}{\sqrt{2\pi}\alpha_{xz0}}\exp\left(-\frac{\alpha_{xz}^2}{2\alpha_{xz0}^2}\right), \tag{3}$$

where α_{xz0} and α_{yz0} are the standard deviations of the distributions, α_{yz} is the included angle between projection of the beam central axis in yz and the projection of ion velocity in yz plane, α_{xz} is the included angle between the projection of beam central axis in xz plane and the projection of the particle velocity in xz plane.

After generating randome numbers α_{xz} and α_{yz} according to the above distribution, each particle gets a specific value of α_{xz} and α_{yz}, which can be used to determine the velocity direction in the local Cartesian coordinates (x, y, z). Denote the angle between $\hat{\mathbf{z}}$ and the projection of the particle velocity in yz plane by α_2. Similarly, denote the angle between $\hat{\mathbf{z}}$ and the projection of particle velocity in xz plane by α_1. These definitions are shown in Fig. 4. Then α_2 is related to α_{yz} by

$$\alpha_2 = \theta_{yz} + \alpha_{yz}, \tag{4}$$

where θ_{yz} is the included angle between the projection of the beam central axis in yz plane and $\hat{\mathbf{z}}$. (For the case shown in Fig. 3, $\theta_{yz} = \theta$ for markers emerging from electrode D, $\theta_{yz} = -\theta$ for markers emerging from electrode A, $\theta_{yz} = 0$ for markers emerging from electrodes B and C.)

Similarly, the angle α_1 is related to α_{xz} by

$$\alpha_1 = \theta_{xz} + \alpha_{xz}, \tag{5}$$

where θ_{xz} is the included angle between projection of the central axis in xz plane and $\hat{\mathbf{z}}$.
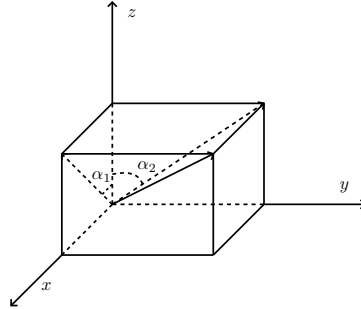

Figure 4. Direction of the particle velocity is determined by α_1 and α_2. Then $v_x/v_z = \tan(\alpha_1)$, $v_y/v_z = \tan(\alpha_2)$.

⟨image|/home/yj/project_new/nbi_fig/fig22/p.eps||||⟩

Figure 5. Cross section of beam at different location.

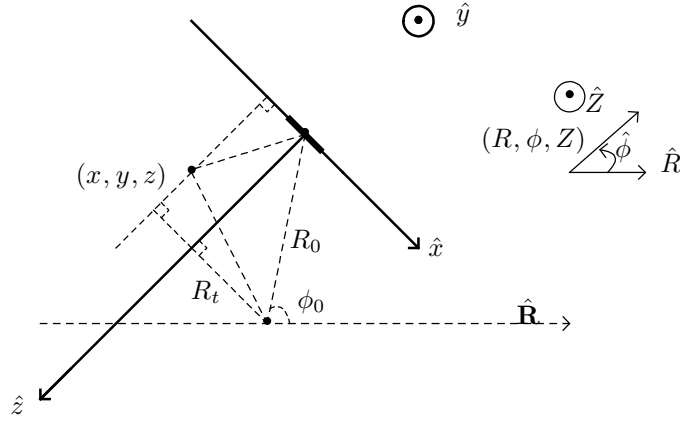## 1.3 Coordinate transform from (x, y, z) to (R, ϕ, Z)

Figure 6. Defintion of the two coordinate systems (x, y, z) and (R, ϕ, Z). The Cartesian coordinates (x, y, z) are used in modeling the injector. In the cylindrical coordinates, the injector center has $(R = R_0, \phi = \phi_0, Z = 0)$. The injector center is the origin of the (x, y, z) Cartesian coordinates. R_t is the tangential radius of the injector, i.e., the perpendicular distance betwen the tokamak center and the center beam line.

1.3.1 Point transform between the two coordinate system

Given Cartesian coordinates (x, y, z), we can calculate the corresponding cylindrical coordinates (R, ϕ, Z) as follows.
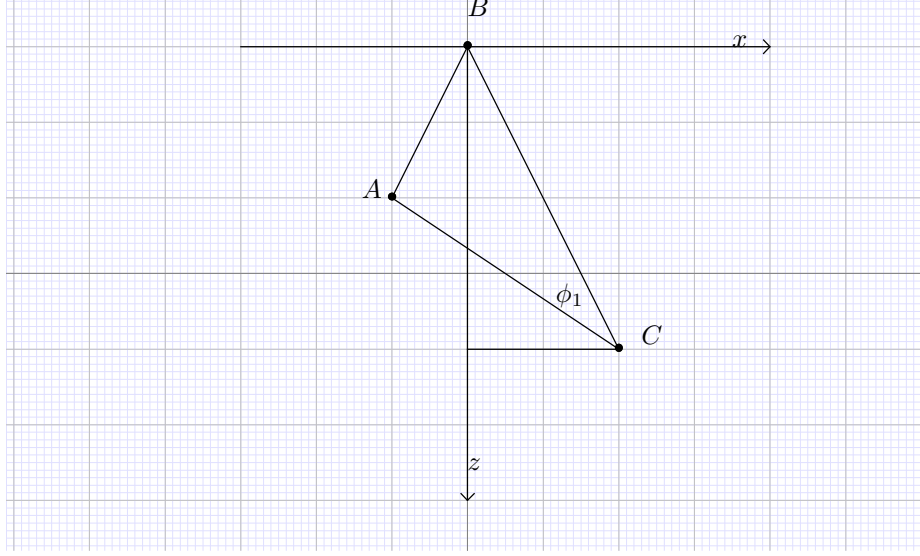

Figure 7. A is the point whose (x, y, z) are known. B is the injector center and C is the tokamak center (i.e., $R = 0$). Note that $z \geqslant 0$ for the points we consider.

$$R = \sqrt{(x_0 - x)^2 + (z_0 - z)^2}, \tag{6}$$

$$Z = y, \tag{7}$$

$$\phi = \phi_0 + \phi_1 \sigma, \tag{8}$$

where (x_0, z_0) is the coordinates of the tokamake center (i.e., $R = 0$) in the Cartesain coordinate system, and is given by

$$z_0 = \sqrt{R_0^2 - R_t^2} \tag{9}$$

$$x_0 = R_{\tan} \sigma_I, \tag{10}$$

σ_I is $+1$ if the injection is anti-clockwise in the top view, otherwise -1. (Anti-clockwise injection corresponds to $\hat{\mathbf{z}}$ pointing to the $+\hat{\phi}$ direction, i.e., the

tokamak center is on the left-hand side if one moves along $\hat{\mathbf{z}}$),

$$\phi_1 = \arccos\left(\frac{R_0^2 + R^2 - (x^2 + z^2)}{2R_0R}\right), \tag{11}$$

$$\sigma = \begin{cases} +1, \text{if } x/z \leqslant x_0/z_0 \\ -1, \text{if } x/z > x_0/z_0 \end{cases} \tag{12}$$

1.3.2 Vector transform between the two coordinate system

The velocity vectors of neutral particles need to be transformed to the cylindrical coordinates:

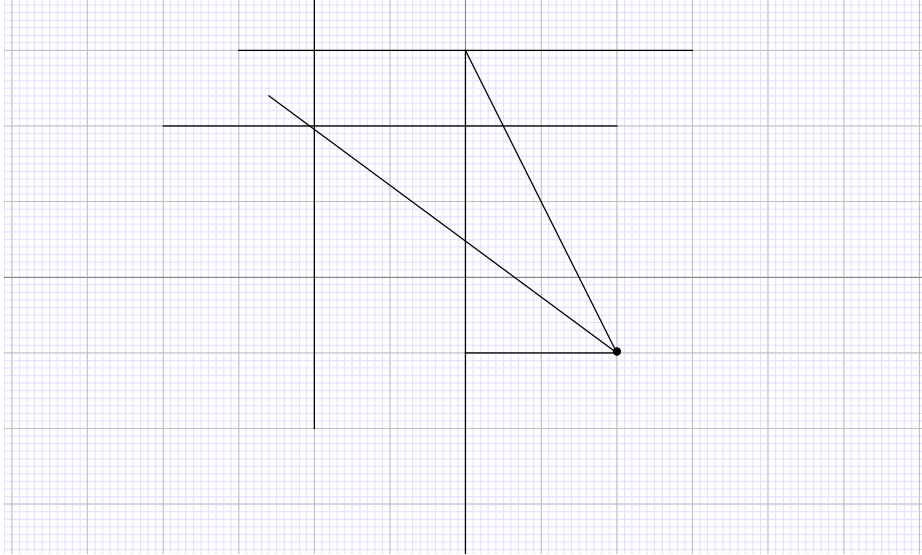$$(v_x, v_y, v_z) \Longrightarrow (v_R, v_\phi, v_Z). \tag{13}$$

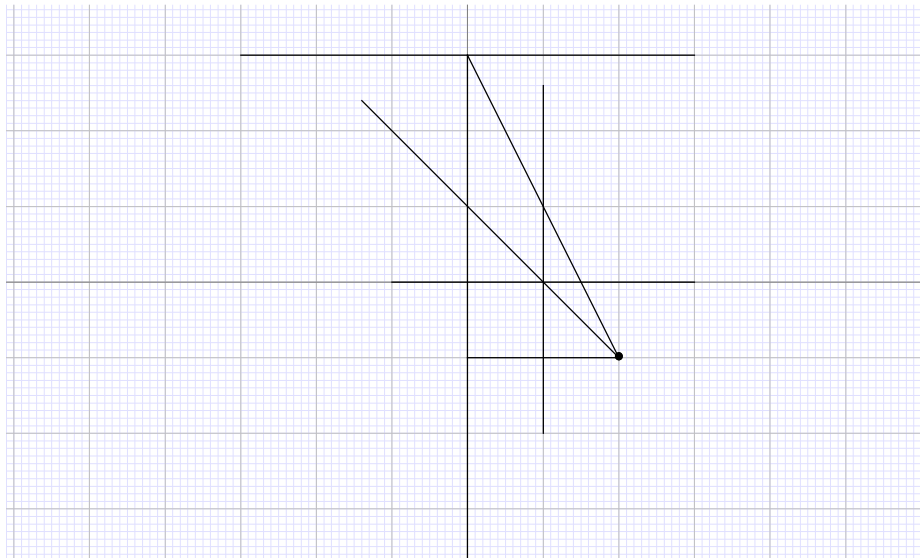**Figure 8.** clockwise injection, case 1
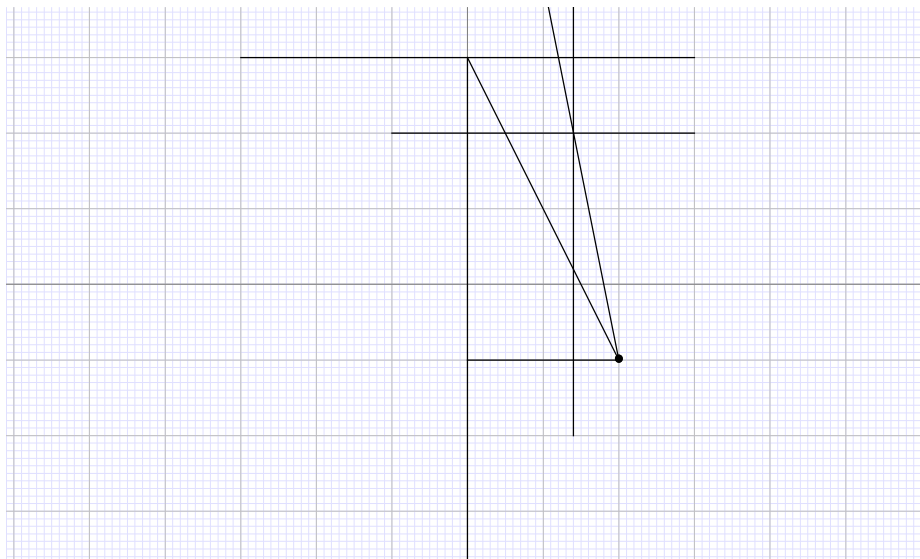
Figure 9. clockwise injection, case 2

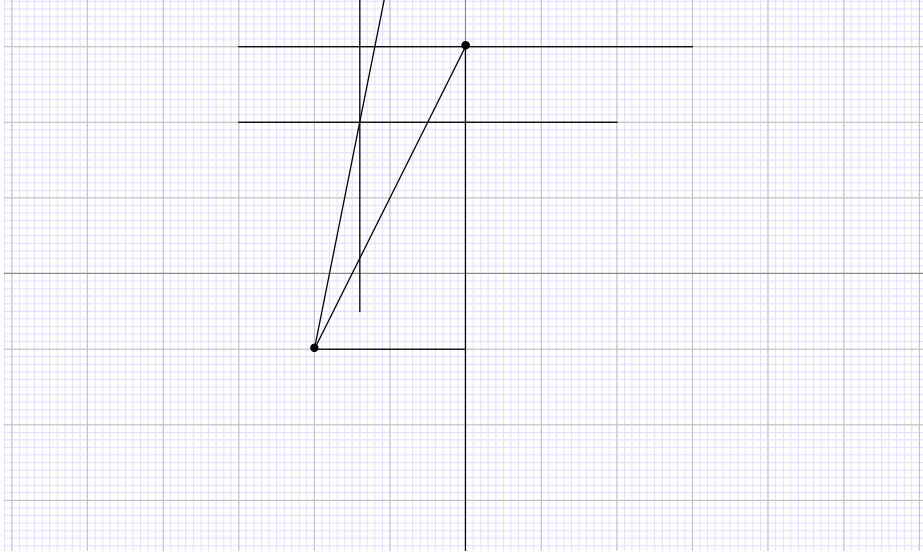**Figure 10.** clockwise injection, case 3

Figure 11. counter-clockwise injection, case 1

$$\angle \mathbf{e}_\phi, (-\mathbf{e}_{v_x}) = \alpha \tag{14}$$

$$\angle \mathbf{e}_\phi, (-\mathbf{e}_{v_z}) = \frac{\pi}{2} - \alpha \tag{15}$$

$$v_\phi = -v_x \cos(\alpha) - v_z \sin(\alpha) \tag{16}$$

$$\angle \mathbf{e}_R, (-\mathbf{e}_{v_z}) = \alpha \tag{17}$$

$$\angle \mathbf{e}_R, (\mathbf{e}_{v_x}) = \frac{\pi}{2} - \alpha \tag{18}$$

$$v_R = v_x \sin(\alpha) - v_z \cos(\alpha) \tag{19}$$

Figure 12. counter-clockwise injection, case 2

Figure 13. counter-clockwise injection, case 3
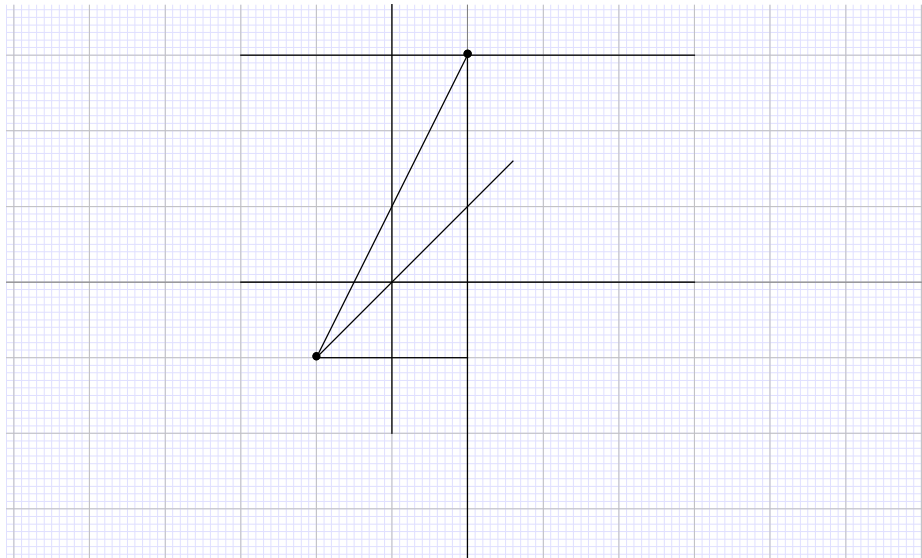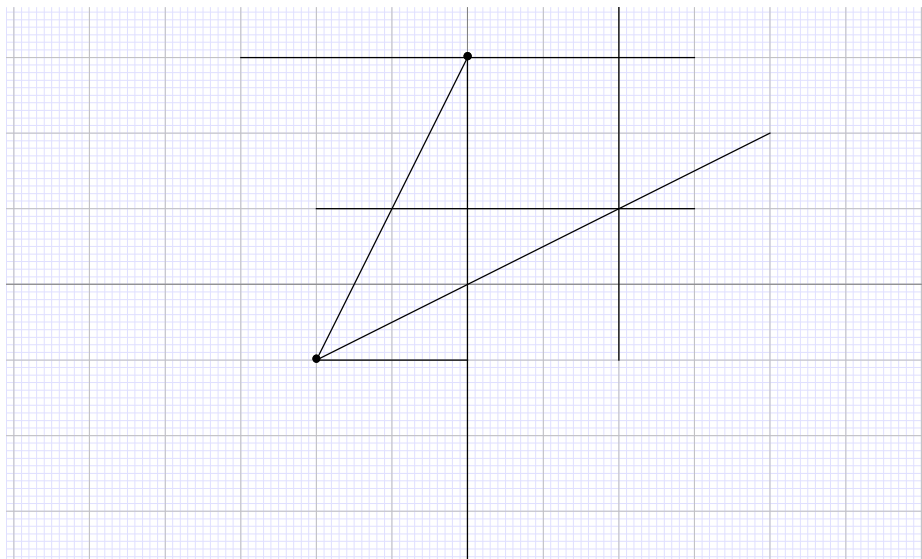
$$\angle \mathbf{e}_R, (\mathbf{e}_{v_x}) = \alpha \tag{20}$$

$$\angle \mathbf{e}_R, (-\mathbf{e}_{v_z}) = \frac{\pi}{2} - \alpha \tag{21}$$

$$v_R = v_x \cos(\alpha) - v_z \sin(\alpha). \tag{22}$$

$$\angle \mathbf{e}_\phi, (-\mathbf{e}_{v_z}) = \alpha \tag{23}$$

$$\angle \mathbf{e}_\phi, (-\mathbf{e}_{v_x}) = \frac{\pi}{2} - \alpha \tag{24}$$

$$v_\phi = -v_x \sin(\alpha) - v_z \cos(\alpha) \tag{25}$$

2 Neutral particle ionization in plasma

When a neutral beam goes through a tokamak plasma, along the trajectory of the beam, the beam intensity is attenuated due to the ionization of neutral particles by the background plasma. The attenuation of beam intensity can be modeled by the following differential equation:

$$\frac{dI}{dl} = -\nu(l)I, \tag{26}$$

where $I(l) = n_b(l)v_b$ is the beam intensity, n_b is the number of beam particles per unit length along the beam trajectory (straight line) and v_b their velocity (assumed to be constant along the trajectory), and $\nu(l)$ is given by

$$\nu(l) = n_i \sigma_{\mathrm{cx}} + n_i \sigma_i + n_e \frac{\langle \sigma_e v_e \rangle}{v_b} \tag{27}$$

where σ_{cx} is the cross-section for charge exchange with plasma ions, σ_i are the cross-section for ionization by plasma ions, $\langle \sigma_e v_e \rangle$ is the electron impact ionization rate coefficient averaged over the Maxwellian distribution ($\langle \sigma_e v_e \rangle / v_b$ is the effective cross-section of electron impact ionization). The dependence of these

cross-sections on the energy of beam particles was given in Fig. 5.3.1 of Wesson's book "Tokamaks" (for reference ease, this figure is included in Appendix A (Fig. 44)). Next section presents the data for the cross-sections I obtain by reading relevant references.

2.1 Ionization cross-sections

2.1.1 Charge exchange

It took me several weeks to try to find up-to-date data for the various ionization cross-sections. I have browsed the data in the ADAS database, which is said to include the most comprehensive and accurate data for the various atom processes in fusion plasmas. However, it seems that some basic information is still lacking in ADAS and some information may be inaccurate or confusing (at lest to me). One example is shown in Fig. 14, where I found the charge-exchange cross-section given in ADAS is too big to be reasonable.
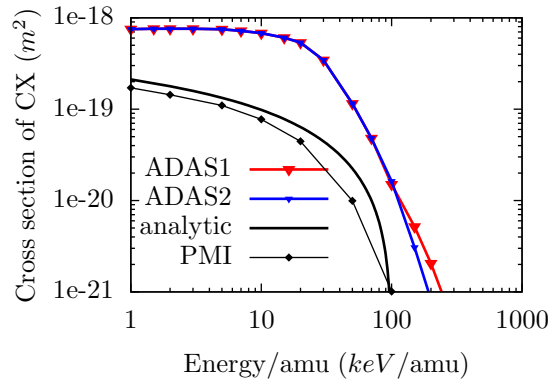

Figure 14. Cross section of charge exchange between Hydrogen-Hydrogen (including the isotopes ^1H, ^2H, and ^3H) as a function of the kinetic energy per amu (atom mass unit) of beam atoms. The data indicated by the blue line and red line are from the ADAS data files "qcx#h0_e2p#h1.dat" and "qcx#h0_e2s#h1.dat", respectively. The results labeled by "PMI" is from the data on Page 78 of Ref. [2]. The analytic fitting results (black line) are from Eq. (28) of Ref. [1], which is given by $\sigma_{ex}(m^2) = 10^{-18}(1 - 0.5(2E)^{0.06} + 4 \times 10^{-7}E)$, where E is the collision energy per amu in eV/amu (update: this fitting formula is not accurate, is not used by me now, a better formula is given in Eq. (28)). The values of the fitting cross section agrees with those given in Fig. 5.3.1 of Wesson's book (Fig. 44 of this report) and these results are almost one order smaller than the results given by ADAS (Presently I do not know the reason. Numerical test indicates neutral beams will deposit at the pedestal of EAST if the ADAS cross section is used, which indicates that ADAS cross section is too big to be reasonable).

A fitting formula given in Page 78 of Ref. [2] is as follows:

$$\sigma_{\mathrm{cx}} = \frac{10^{-20} A_1 \ln(A_2 / E + A_6)}{1 + A_3 E + A_4 E^{3.5} + A_5 E^{5.4}}, \tag{28}$$

where σ_{cx} is expressed in m^2 and E is in keV $/$ amu, $A_1 = 3.2345$, $A_2 = 235.88$, $A_3 = 0.038371$, $A_4 = 3.8068 \times 10^{-6}$, $A_5 = 1.1832 \times 10^{-10}$, $A_6 = 2.3713$.
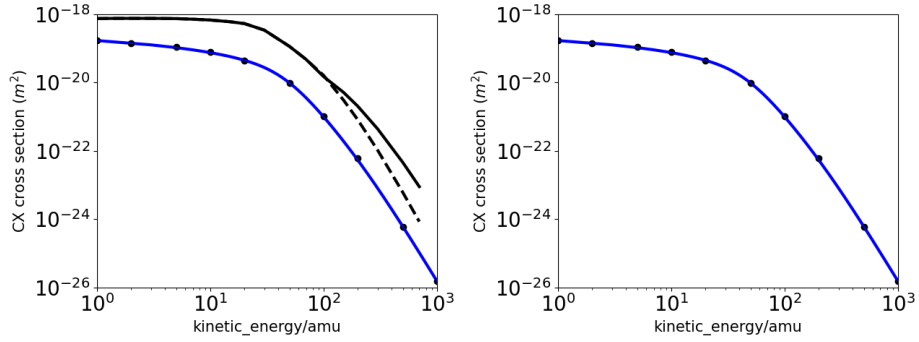

Figure 15. Blue line is from Eq. (28). black dot is from the data on Page 78 of Ref. [2]. The data indicated by the black solid line and dashed line are from the ADAS data files "qcx#h0_e2p#h1.dat" and "qcx#h0_e2s#h1.dat", respectively.

2.1.2   Ion impaction ionization

I can not find the data of the ion impaction ionization cross section from the ADAS database. It seems that there are very few papers discussing the ion impaction ionization cross section. One of the papers I found useful is Kaganovich's paper[3], which gives the following fitting formula for the impaction ionization cross section by a fully stripped ion:

$$\sigma_i(v, I_{\mathrm{nl}}, Z_p) = \pi a_0^2 \frac{N_{\mathrm{nl}} Z_p^2}{(Z_p + 1)} \frac{E_0^2}{I_{\mathrm{nl}}^2} G^{\mathrm{new}}\!\left(\frac{v}{v_{\mathrm{nl}}\sqrt{Z_p + 1}}\right), \tag{29}$$

where v is the relative velocity between the atom and the ion, Z_p is the atomic number of the fully stripped ion, I_{nl} is the ionization potential of the atom,

$v_{\mathrm{nl}} = v_0\sqrt{2I_{\mathrm{nl}}/E_0}$ with $v_0 = 2.2\times10^6 m/s$ and $E_0 = 27.2$eV, N_{nl} is the number of electrons in the nl orbital of the atom ($N_{\mathrm{nl}} = 1$ for hydrogen), $a_0 = 0.529\times10^{-10}m$ is the Bohr radius, and

$$G^{\mathrm{new}} = \frac{1}{x^2}\exp\left(-\frac{1}{x^2}\right)[1.26 + 0.283\ln(2x^2 + 25)]. \qquad (30)$$
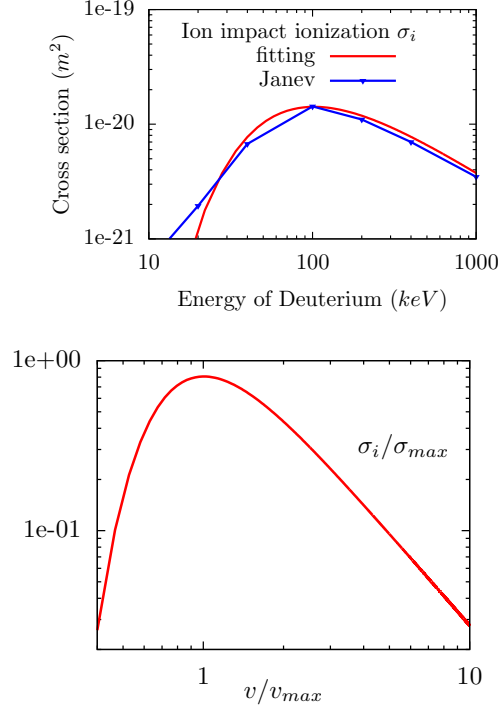

Figure 16. Left: Cross section of ion impact ionization of deuterium as a function of the kinetic energy of deuterium atom (red line is calculated by using Eq.(29), blue line is for the data given in Page 68 of Ref. [2]). Right: Normalized cross section $\sigma_i/\sigma_{\max}$ as a function of the normalized velocity $v/v_{\max}$, where $\sigma_{\max} = \pi a_0^2 Z_p^2/(Z_p+1)E_0^2/I_{\mathrm{nl}}^2$, $v_{\max} = v_{nl}\sqrt{Z_p+1}$. These results agree with Fig. 3 of Kaganovich's paper[3].

For neutral beam injection relevant to present tokamaks, the thermal velocity of plasma ions are much smaller than the velocity of beam atoms, i.e., $v_{ti} \ll v_b$, so that $v_{ti} \approx 0$ can be assumed. As a result, σ_{ch} and σ_i discussed above are independent of the temperature of the background plasma ions. However,

the electron impact ionization rate coefficient $\langle\sigma_e v_e\rangle$ usually depends on the temperature of background electrons because the thermal velocity of electrons is usually comparable to the beam velocity and an averaging over the electron Maxwellian distribution is needed. The dependence of the electron ionization rate coefficient $\langle\sigma_e v_e\rangle$ on the electron temperature is plotted in Fig. 17.
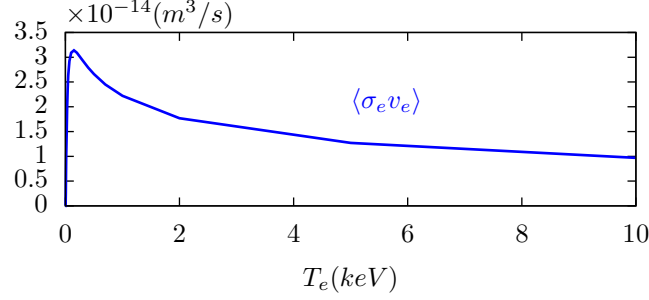

Figure 17. The dependence of the electron impact ionization rate coefficient $\langle\sigma_e v_e\rangle$ on the electron temperature T_e. These data are obtained by using the open-ADAS reading program "xxdata_07" to acces the ADAS data file "szd93#h_h0.dat", which stores the electron ionization rate coefficient for hydrogen atom.
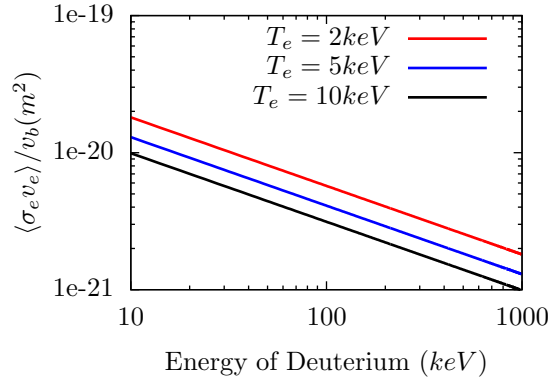

Figure 18. The dependence of the electron impact ionization cross section $\langle\sigma_e v_e\rangle/v_b$ on the kinetic energy of the Deuterium atom for the three cases with $T_e = 2$keV, 5keV, and 10keV.

Presently, multi-step ionization processes are not incorporated in my code. Ionization cross section due to the contribution of impurity ions are also not

included.

2.2 Monte-Carlo implementation of beam attenuation (fast ions generation)

The solution to Eq. (26) can be analytically obtained, which is given by

$$I = I_0 e^{-\int_0^l \nu(l')dl'}, \tag{31}$$

where I_0 is the beam density at the starting point of the beam trajectory. The solution (31) indicates an exponential attenuation of the beam intensity along the beam trajectory.

The Mote-Carlo method of implementing the beam attenuation due to ionization process is as follows. First load assemble of neutral particles with each particle associated with a uniform random number η in the range of [0, 1]. Along the trajectory of each neutral particle (straight line), the integration $s = \int_0^l \nu(l')dl'$ is calculated to examine whether $s \geqslant \ln(1/\eta)$ or not. If $s \geqslant \ln(1/\eta)$, then the neutral particle is considered to be ionized. A simple numerical experiment can verify that this implementation generate results in agreement with the analytic solution given by Eq. (31).

Those neutral particles that are not yet ionized when they reach the inner wall of the device are usually lost to the wall and this loss of neutral particles are called shine-through loss. The shine-through loss is usually very small on large machine like ITER but for a medium-size tokamak like EAST, shine-through loss can be large, especially for the more perpendicular beam and lower-density plasmas.

To represent the neutral particles source from the injector, an assemble of neutral particles are loaded with desired distribution over energy and direction of velocity. Due to the presence of dual-atom and tri-atom molecules in the accelerator, single-atom neutral particles injected into tokamaks have three possible energies E, $E/2$ and $E/3$. Energy distribution over these three energies is implemented. For EAST ion source, the number ratio between particles with full-energy, half-energy and third energy is $n_f/n_{f/2}/n_{f/3} = 80:14:6$. The spatial distribution of neutral particles on the injector surface are also implemented by assuming a bi-gaussian distribution along the vertical and horizontal directions
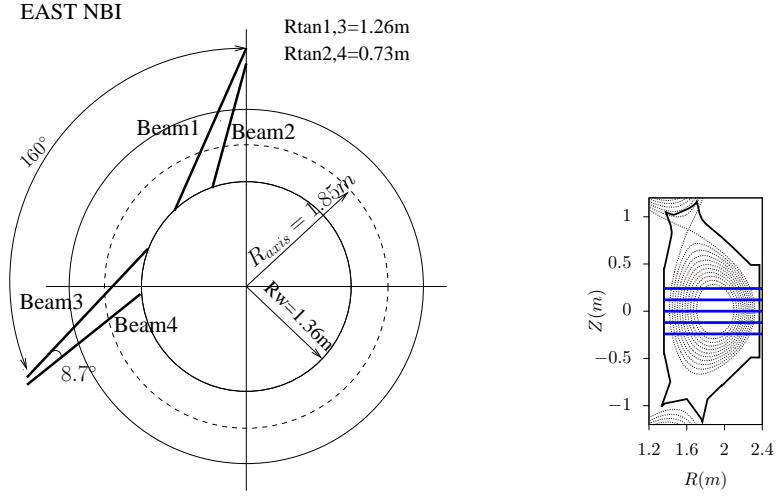
(check, density vs. intensity).

EAST NBI

Rtan1,3=1.26m
Rtan2,4=0.73m

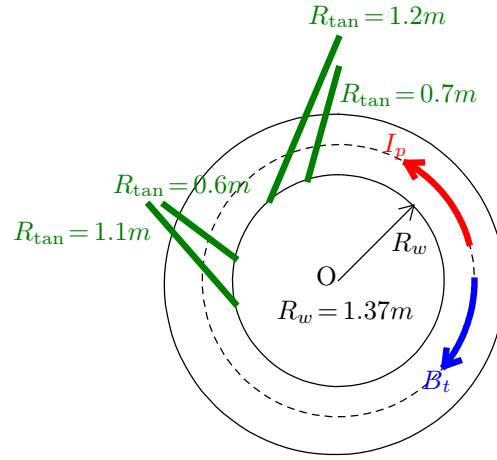**Figure 19.** Top view (left) and poloidal view (right) of neutral beam lines on EAST.

Figure 20. 2021 updated, Top view (left) of neutral beam lines on EAST.

3 Benchmarking the new code with NUBEAM code

To verify the reliability of the new code, we have performed a benchmarking case with the NUBEAM code of PPPL. The plasma density and temperature profiles used in the benchmarking case are shown in Fig. 21.

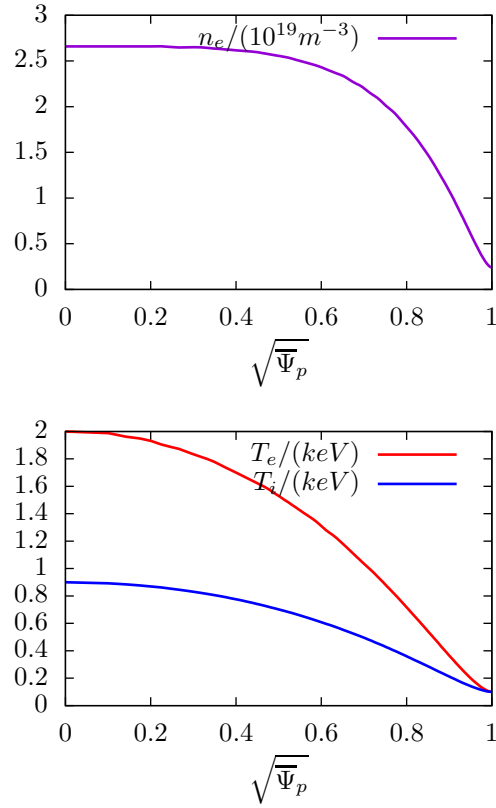**Figure 21.** Profiles of number density of electrons (left) and temperature of electrons and ions (right) used in the benchmarking case. These profiles were provided by Baolong Hao for modeling the profiles of EAST discharge #59954@3.0s

The ionization cross-sections used in the new code, which is given in Sec., do not include the contributions from multi-step ionization process. Multi-step ion-

ization refers to the case where a collision push a neutral into its excited state and
a subsequent collision revmove the electron from the neutral before the elecron
decays to its ground state. NUBEAM include the excited state correction due to
this multi-step ionization and this correction is turned off in the benchmarking
case. Furthermore, the ionization due to collsion with impurities is not included
in the new code and is turned off in NUBEAM in the benchmarking case. The
comparison of the beam density deposition profiles calculated by the new code
and NUBEAM code are shown in Fig. 22.
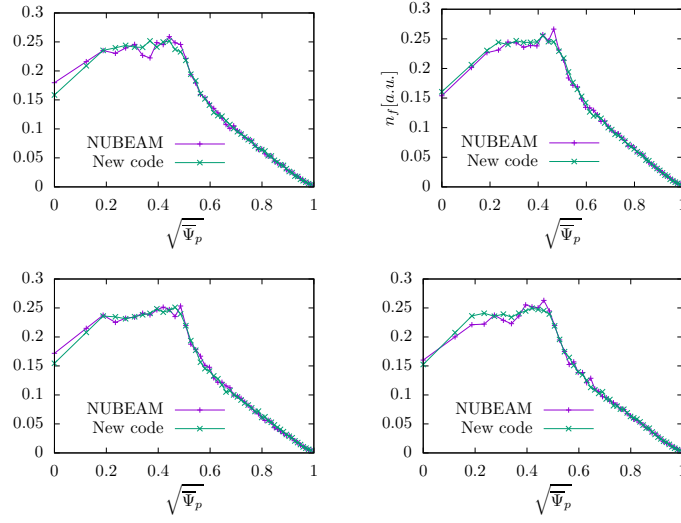
Figure 22. Comparison of the beam density deposition profiles calculated by the
new code and NUBEAM code. upper left: $R_{\tan} = 0.731m$, upper right: $R_{\tan} = 0.606m$,
lower left: $R_{\tan} = 1.26m$, lower right:$R_{\tan} = 1.141m$,
    gfile used is "g059954.003030", profiles used are at 3.0s, as shown in Fig. 21. The
NUBEAM results were provided by Baolong Hao.

Figure 23 is the same as Fig. 22 except that the excited state correction due
to multi-step ionization is included NUBEAM.
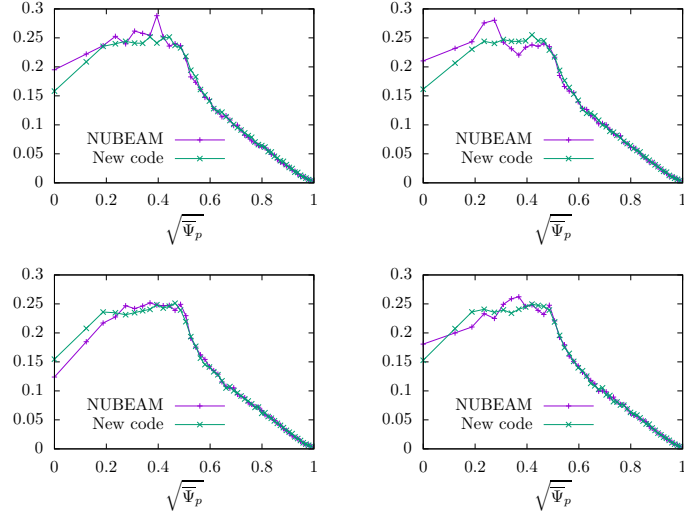
Figure 23. The same as Fig. 22 except that the excited state correction due to multi-step ionization is included NUBEAM.

upper left: $R_{\tan} = 0.731m$, shine-through-loss=0.325599, Baolong's result: 0.3149

upper right: $R_{\tan} = 0.606m$, shine-through-loss=0.336283333, Baolong's result: 0.32525

lower left: $R_{\tan} = 1.26m$, shine-through-loss=0.23769, Baolong's result: 0.2268

lower right:$R_{\tan} = 1.141m$, shine-through-loss=0.26634. Baolong's result: 0.25625
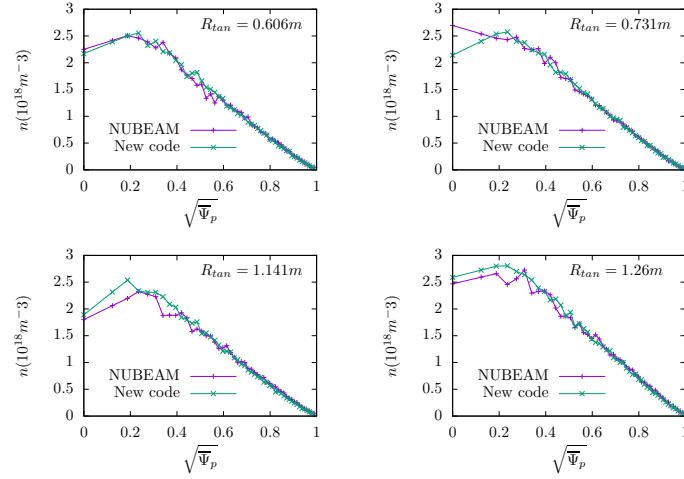
Figure 24. Flux-surface averaged densities of ionized neutrals. The effects of beam focus and divergence, and the aperture size are included.

4 Numerical results

4.1 Equilibrium profiles
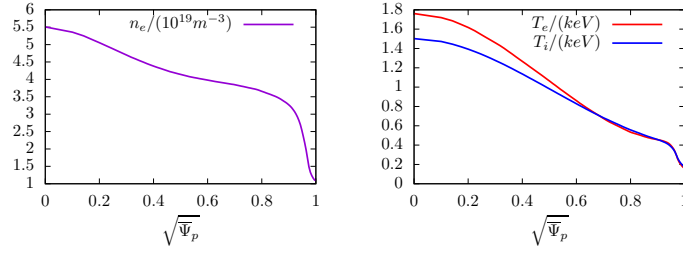
Figure 25. Profiles of number density of electrons (left) and temperature of electrons and ions (right) of EAST discharge #62585@2.8s.
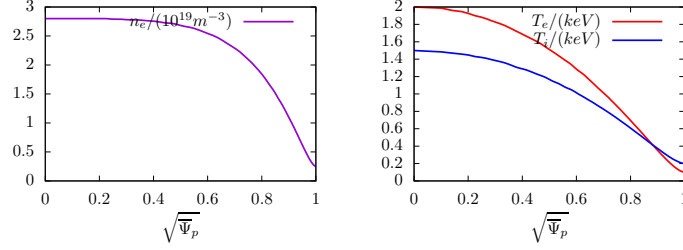
Figure 26. Profiles of number density of electrons (left) and temperature of electrons and ions (right) of EAST discharge #59954@3.2s

4.2 Spatial distribution of fast ions generated by neutral beam injection

The shine-through time of a neutral particle ($4 \times 10^{-7}s$ for 50keV neutral beam on EAST) is much shorter than the typical poloidal orbit period ($\sim 4 \times 10^{-5}s$). Therefore the time difference between the birth of various fast ions is tiny and

thus can be neglected, i.e., all the fast ions can be considered to be born at the same time.
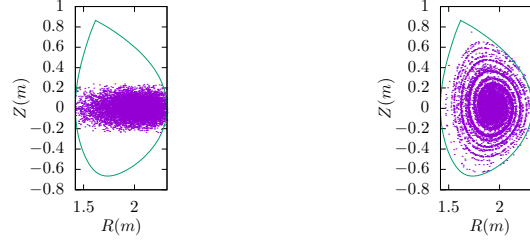
Figure 27. Poloidal view of the locations of fast ions at birth (left) and 0.078ms later (right) due to neutral beam particles of 50keV injected to EAST tokamak from a rectangular source with heigh of 0.12m and width of 0.48m. The tangency radius of the central beam of the source is $0.73m$. The central beam is on the midplane and the divergence of the beams is neglected. Magnetic configuration is from EAST discharge #62585@2.8s (gfile provided by ZhengZheng). The electron density profile is plotted in Fig. 25.

⟨image|/home/yj/project_new/guiding_center_motion/fig24e/p.eps||||⟩
⟨image|/home/yj/project_new/guiding_center_motion/fig24d/p.eps||||⟩

Figure 28. Top view of the locations of fast ions at birth (left) and 0.078ms later (right) due to neutral beam particles of 50keV injected to EAST tokamak from a rectangular source with heigh of 0.12m and width of 0.48m. The tangency radius of the central beam of the source is $0.73m$. The central beam is on the midplane and the divergence of the beams is neglected. Magnetic configuration is from EAST discharge #62585@2.8s (gfile provided by ZhengZheng).
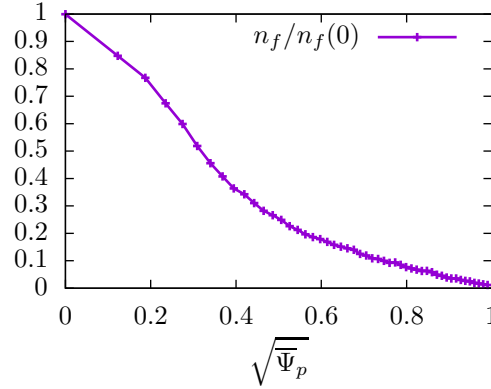
Figure 29. Density profiles of initially deposited NBI fast ions.

4.3 Loss of fast ions to the wall

⟨image|/home/yj/project_new/nbi_fig/fig2b/figa/p.eps||||⟩
⟨image|/home/yj/project_new/nbi_fig/fig2b/figc/p.eps||||⟩

⟨image|/home/yj/project_new/nbi_fig/fig2b/figb/p.eps||||⟩
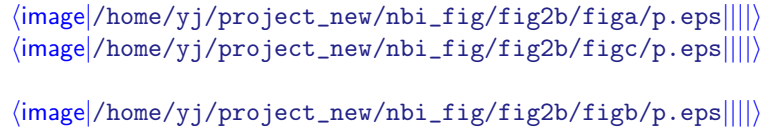
Figure 30. Comparison of fast ions loss fraction due to counter-current NBI and co-current NBI in EAST discharge #62585@2.8s. Maximal energy is 50keV. The central beam is on the midplane with the tangency radius being $0.73m$ (left figure) and $1.26m$ (right figure).

⟨image|/home/yj/project_new/nbi_fig/fig2/figa/p.eps||||⟩
⟨image|/home/yj/project_new/nbi_fig/fig2/figc/p.eps||||⟩
⟨image|/home/yj/project_new/nbi_fig/fig2/figb/p.eps||||⟩
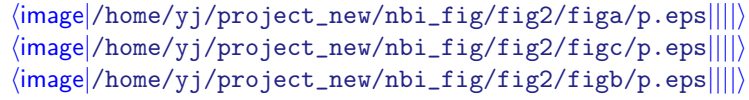
Figure 31. The same as Fig. 30 but with FLR effect included.in EAST discharge #62585@2.8s.

⟨image|/home/yj/project_new/nbi_fig/fig3/p.eps||||⟩
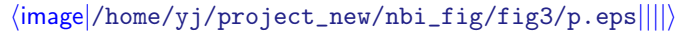
Figure 32. Rtan=0.73m. cntr-Ip. in EAST discharge #62585@2.8s.
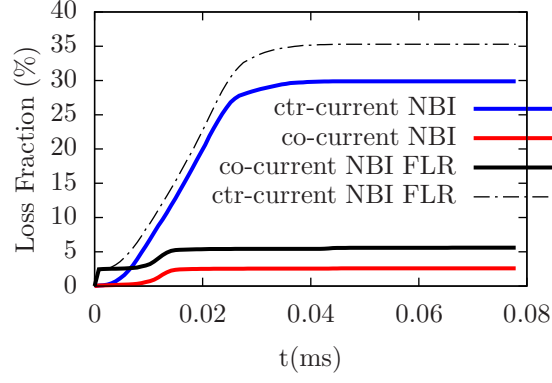
Figure 33. Comparison of fast ions prompt loss fraction in EAST discharge #62585@2.8s. Maximal energy is 50keV. The central beam is on the midplane with the tangency radius being $0.73m$. LCFS is used as the loss boundary
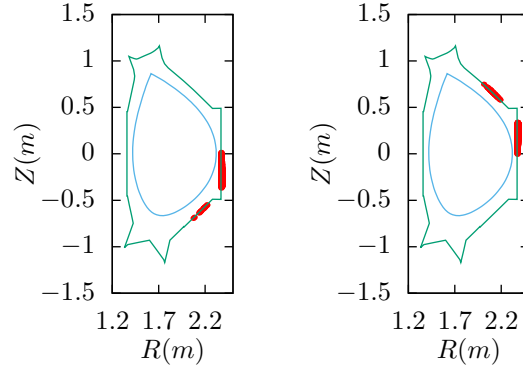
Figure 34. Distribution of the lost fast ions on the first wall for the case $B_\phi < 0$ (left) and $B_\phi > 0$ (right). Neutral beam is injected in $+\hat{\phi}$ direction, which is in the counter-current injection. The magnetic configuration is from EAST discharge #62585@2.8s (gfile provided by ZhengZheng).
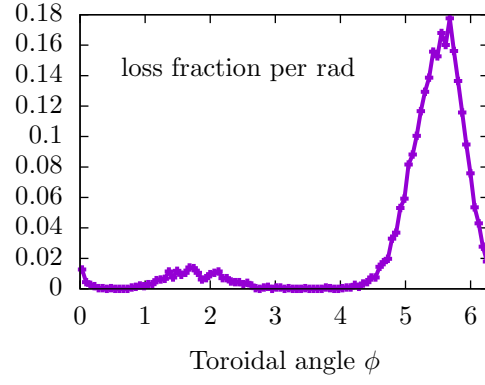
Figure 35. Toroidal distribution of lost fast ions
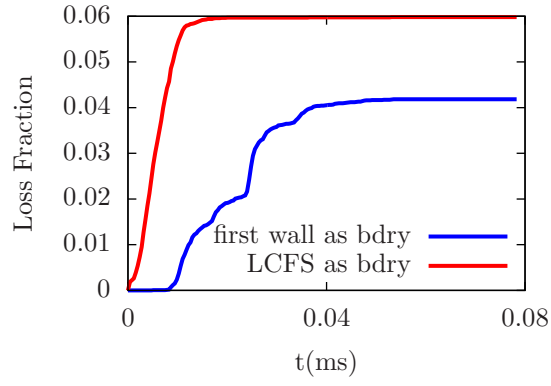
Figure 36. Comparison of fast ions loss fraction due to counter-current neutral beam injection in EAST discharge #62585@2.8s calculated using (a) the first wall of the machine and (b) the last-closed-flux-surface (LCFS) as the loss boundary.

5 Effects of RMP on confinement of NBI fast ions
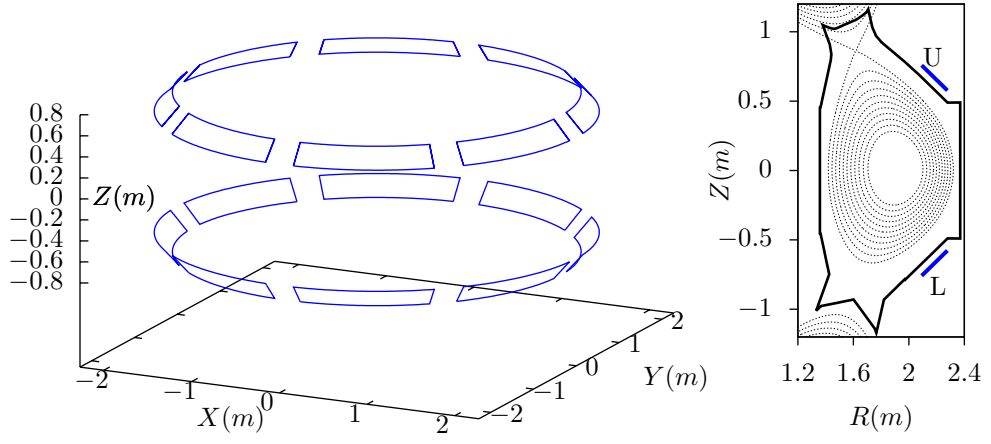
Figure 37. Location of the RMP coils on EAST tokamak in 3D view (left) and poloidal view (right).
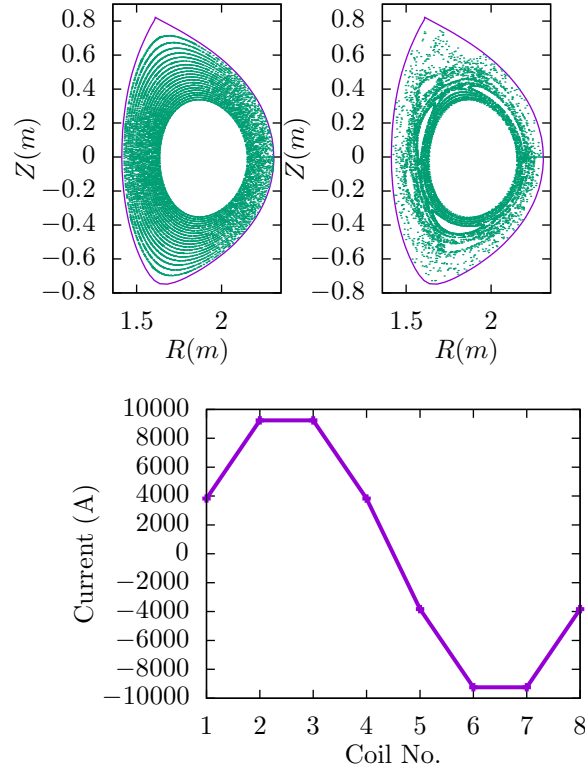
Figure 38. Poincare section of magnetic field lines of axisymmetric magnetic field (left) and the superpostion of the axisymmetric magnetic field and a magnetic perturbation generated by RMP coils (middle). Right: current in each RMP coil. The axisymmetric magnetic field is from EAST discharge #59954@3.1s. These Poincare sections are obtained by tracing 20 field lines starting from 20 points on the the low-field-side midplane, and then then recording the intersecting points of these field lines with the $\phi = 0$ plane. The maximum number of intersecting points for each field line is set to 700. In (a), i.e. axisymetrica field, the Poincare points form nested surface, which inidcates the accuracy of the field line tracing is good. In (b), some field lines touch the first wall of the machine before they finish 700 toroidal turns.
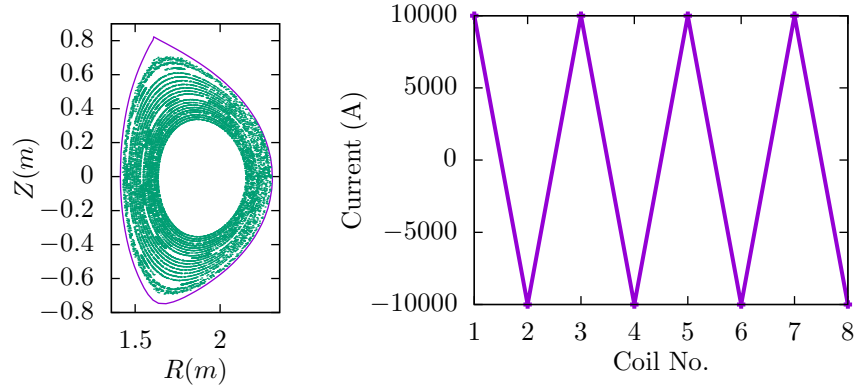
Figure 39. Left: Poincare section of magnetic field lines. Right: current in each upper-RMP coils (the current in lower-RMP coils are identical with that of the corresponding upper coil).

⟨image|/home/yj/project_new/nbi_fig/fig8/p.eps||||⟩
⟨image|/home/yj/project_new/nbi_fig/fig8b/p.eps||||⟩

Figure 40. (1)Rtan=1.264m, (2) Rtan=0.731, co-Ip, in EAST discharge #59954@3.2s

⟨image|/home/yj/project_new/nbi_fig/fig8c/p.eps||||⟩
⟨image|/home/yj/project_new/nbi_fig/fig8f/p.eps||||⟩

Figure 41. (1)Rtan=1.414m (2) Rtan=0.606, cntr-Ip, in EAST discharge #59954@3.2s

⟨image|/home/yj/project_new/nbi_fig/fig8e/p.eps||||⟩

Figure 42. Rtan=0.606, cntr-Ip , in EAST discharge #59954@3.2s

5.1 Fast ion collisional friction due to background Maxwellian ions and electrons

The collision friction coefficient due to an isotropic background distribution is given by[4]

$$F^{a/b}(v) = -\frac{4\pi\Gamma^{a/b}}{3n_b}\frac{m_a}{m_b}\frac{1}{v^2}\int_0^v 3(v')^2 f_b(v')dv', \tag{32}$$

where

$$\Gamma^{a/b} = \frac{n_b q_a^2 q_b^2}{4\pi\epsilon_0^2 m_a^2}\ln\Lambda^{a/b}. \tag{33}$$

The velocity of the fast ions from NBI is much larger than the thermal velocity of ions but still much smaller than the electron thermal velocity, i.e,

$$v_{ti} \ll v_f \ll v_{te}. \tag{34}$$

Under theabove conditions, the fast ion collision terms due to background ions and electrons can be simplified.

[For the 3.5MeV α particles created by D-T reaction in ITER plasmas, the relation in Eq. (34) also applies. The ratio of α particle's velocity to v_{te} is given by

$$\frac{v_\alpha}{v_{te}} = \sqrt{\frac{T_\alpha}{T_e}\frac{m_e}{m_\alpha}}. \tag{35}$$

For an electron temperature $T_e = 20$keV, the above equation gives

$$\frac{v_\alpha}{v_{te}} = \sqrt{\frac{3.5\times10^6\text{eV}}{20\times10^3\text{eV}}\frac{1}{1836}} = 0.304, \tag{36}$$

which indicates that the velocity of α particles is still smaller than the electron thermal velocity.]

5.1.1 Collisional friction with background ions

Consider the collision friction of fast ions with thermal ions. Assume the distribution of thermal ions is Maxwellian, then Eq. (32) is written

$$F^{f/i}(v) = -\frac{4\pi\Gamma^{f/i}}{3n_i}\frac{m_f}{m_i}\frac{1}{v^2}\int_0^v 3(v')^2 f_{Mi}(v')dv', \tag{37}$$

where

$$f_{Mi} = n_i\left(\frac{m_i}{2\pi T_i}\right)^{3/2}\exp\left(-\frac{v^2}{v_{ti}^2}\right), \tag{38}$$

with $v_{ti} = \sqrt{2T_i/m_i}$. Since v_f is much larger than the thermal velocity of ions, the collision friction coefficients can be approximated by the high-velocity-limit (i.e. setting the upper limit of the integration to be $+\infty$), which gives

$$
\begin{aligned}
F^{f/i}(v) &= -4\pi\Gamma^{f/i}\frac{m_f}{m_i}\frac{1}{v^2}\left(\frac{m_i}{2\pi T_i}\right)^{3/2}v_{ti}^3\frac{\sqrt{\pi}}{4}\\
&= -\Gamma^{f/i}\frac{m_f}{m_i}\frac{1}{v^2},
\end{aligned}
\tag{39}
$$

which indicates that $F^{f/i} \propto 1/v^2$.

There are usually multiple ion species in tokamak plasmas. The total friction is then written as

$$\sum_i F^{f/i}(v) = -\frac{m_f}{v^2} \sum_i \frac{\Gamma^{f/i}}{m_i}. \tag{40}$$

The corresponding slowing-down time is written as

$$t_s^{(\text{ai})} \equiv \frac{v}{|\sum_i F^{f/i}|} = \frac{v^3}{m_f \sum_i \frac{\Gamma^{f/i}}{m_i}}, \tag{41}$$

and the slowing-down rate $\nu_s^{(\text{ai})}$ is written as

$$\nu_s^{(\text{ai})} \equiv \frac{1}{t_s^{(\text{ai})}} = \frac{\sum_i \frac{\Gamma^{f/i}}{m_i} m_f}{v^3}. \tag{42}$$

5.1.2 Collisional friction with background electrons

Next, consider the collision friction of fast ions with background electrons. Assume the distribution of electrons is Maxwellian, then Eq. (32) is written

$$
\begin{aligned}
F^{f/e} &= -\frac{4\pi\Gamma^{f/e}}{n_e} \frac{m_a}{m_e} \frac{1}{v^2} \int_0^v (v')^2 f_{Me}(v') dv' \\
&= -\frac{4\pi\Gamma^{f/e}}{n_e} \frac{m_a}{m_e} \frac{1}{v^2} \int_0^v (v')^2 n_e \left(\frac{m_e}{2\pi T_e}\right)^{3/2} \exp\left(-\frac{v'^2}{v_{te}^2}\right) dv' \\
&= -4\pi\Gamma^{f/e} \left(\frac{m_e}{2\pi T_e}\right)^{3/2} \frac{m_a}{m_e} \frac{v_{te}^3}{v^2} \int_0^x x'^2 \exp(-x'^2) dx',
\end{aligned}
\tag{43}
$$

where $x' = v'/v_{te}$ and $x = v/v_{te}$. Since $v_f \ll v_{te}$ and thus $x \ll 1$, we adopt the approximation $e^{-x'^2} \approx 1$. Then Eq. (43) is written

$$
\begin{aligned}
F^{f/e} &= -4\pi\Gamma^{f/e} \left(\frac{m_e}{2\pi T_e}\right)^{3/2} \frac{m_f}{m_e} \frac{v_{te}^3}{v^2} \int_0^x (x'^2) dx' \\
&= -4\pi\Gamma^{f/e} \left(\frac{m_e}{2\pi T_e}\right)^{3/2} \frac{m_f}{m_e} \frac{v_{te}^3}{v^2} \left(\frac{x^3}{3}\right) \\
&= -4\pi\Gamma^{f/e} \left(\frac{m_e}{2\pi T_e}\right)^{3/2} \frac{m_f}{m_e} \frac{v}{3},
\end{aligned}
\tag{44}
$$

which indicates that $F^{f/e} \propto v$.

The slowing down time $t_s^{(e)}$ is defined by

$$t_s^{(e)} = \frac{v}{|F^{f/e}|} = -\frac{v}{F^{f/e}}, \tag{45}$$

which, by using Eq. (44), is written

$$t_s^{(e)} = \frac{3\sqrt{\pi}}{4} \frac{m_e}{m_f} \frac{v_{te}^3}{\Gamma^{f/e}}. \tag{46}$$

The corresponding slowing-down rate is written as

$$\nu_s^{(e)} = \frac{1}{t_s^{(e)}} = \frac{4}{3\sqrt{\pi}} \frac{m_f}{m_e} \frac{\Gamma^{f/e}}{v_{te}^3}. \tag{47}$$

Equation (46) agrees with the slowing down time given in Ref. [7] (the formula after Eq. (1) of Ref. [7]). Note that this frequency is independent of the velocity of fast ions.

Inserting expression (33) of $\Gamma^{f/e}$ into Eq. (46), we obtain

$$t_s^{(e)} = \frac{3(2\pi)^{3/2} T_e^{3/2} \epsilon_0^2}{n_e Z_f^2 e^4 \ln\Lambda^{f/e}} \frac{m_f}{\sqrt{m_e}}. \tag{48}$$

Note that the slowing down time $t_s^{(e)}$ is proportional to $T_e^{3/2}/n_e$. Both T_e and n_e decrease from tokamak core to edge. Usually, $T_e^{3/2}$ dependence wins over n_e, making $t_s^{(e)}$ be decreasing from the core to the edge.

Also note that the slowing down time given by Eq. (46) is independent of the velocity of fast ions. For EAST parameters $T_e = 2\text{keV}$, $n_e = 4 \times 10^{19} m^{-3}$, the slowing down time of a fast Deuterium ion calculated by Eq. (46) is $t_s = 565\text{ms}$. However, this value is usually significantly different from the real slowing-down time for two reasons. First, this is just a characteristic slowing-down time rather than a slowing-down time obtained from solving the differential equation. Second, the friction of fast ions with the thermal ions is not taken into account. Therefore, more accurate value of slowing down time (Eq. (84)) on EAST is much shorter than the 565ms given above, e.g. 50ms.

5.1.3   Critical velocity

The critical velocity v_c is defined as the fast ion velocity at which its friction with the background ions is equal to that with the electrons , i.e. $\sum_i F^{f/i} = F^{f/e}$. Using this, along with Eqs. (39) and (44), we obtain

$$-\frac{m_f}{v_{\text{crit}}^2} \sum_i \frac{\Gamma^{f/i}}{m_i} = -4\pi \Gamma^{f/e} \left(\frac{m_e}{2\pi T_e} \right)^{3/2} \frac{m_f}{m_e} \frac{v_c}{3}, \tag{49}$$

which can be written as

$$v_c = v_{te} \left(\frac{3\sqrt{\pi}}{4} \frac{\sum_i \frac{\Gamma^{f/i}}{m_i}}{\frac{\Gamma^{f/e}}{m_e}} \right)^{1/3}. \tag{50}$$

Noting that $\Gamma^{a/b} = \frac{n_b q_a^2 q_b^2}{4\pi\epsilon_0^2 m_a^2} \ln\Lambda^{a/b}$ and $\ln\Lambda^{f/i} \approx \ln\Lambda^{f/e}$, the above expression is written as

$$v_c = v_{te} \left(\frac{3\sqrt{\pi}}{4} \sum_i \frac{m_e n_i Z_i^2}{m_i n_e} \right)^{1/3}. \tag{51}$$

where $Z_i = q_i/e$ is the charge number of ion species i. Note that the critical velocity is solely determined by the bakground plasma, and is independent of the fast ion mass and charge number. Also note that, due to the ion mass dependence, the sum over the background ion species can not be written in terms of $Z_{\mathrm{eff}} = \sum_i n_i Z_i^2 / n_e$. Define

$$Z_m = \sum_i \frac{m_e n_i Z_i^2}{m_i n_e}, \tag{52}$$

then expression (51) is written as

$$v_c = v_{te} \left(\frac{3\sqrt{\pi}}{4} Z_m \right)^{1/3}. \tag{53}$$

[Since Tungsten ($Z = 74$) is only partially stripped at typical fusion electron temperatures[[?]], we choose an average charge state of $Z_W = 50$.

$$n_T + n_D + 2n_{\mathrm{He}} + Z_W n_W = n_e$$

$$n_T + n_D + n_{\mathrm{He}} \times 2^2 + n_W Z_W^2 = Z_{\mathrm{eff}} n_e$$

$$-n_T - n_D + n_W(Z_W^2 - 2Z_W) = (Z_{\mathrm{eff}} - 2)n_e$$

$$n_W = \frac{n_T + n_D + (Z_{\mathrm{eff}} - 2)n_e}{Z_W^2 - 2Z_W} \tag{54}$$

$$n_{\mathrm{He}} = \frac{n_e - n_T - n_D}{2} - \frac{Z_W}{2} n_W \tag{55}$$

]

[For Deuterium plasmas with impurities that are of the same charge mass ratio as Deuterium and are fully stripped, then $m_D Z_i / m_i = 1$ for all ion species. Using this along with the charge neutrality condition $n_e = \sum_i n_i Z_i$, expression (51) can be simplified as

$$v_c = v_{te} \left(\frac{3\sqrt{\pi}}{4} \frac{m_e}{m_D} \right)^{1/3}. \tag{56}$$

]

[If there is only one species of ions and we assume the charge neutrality, i.e., $n_i Z_i = n_e$, then expression (51) is written as

$$v_c = v_{te} \left(\frac{3\sqrt{\pi}}{4} \frac{m_e}{m_i} Z_i \right)^{1/3}, \tag{57}$$

The corresponding fast ions kinetic energy is written as

$$E_c \equiv \frac{1}{2} m_f v_c^2 = \frac{m_f}{m_i} \left(\frac{m_i}{m_e} \right)^{1/3} \left(Z_i \frac{3\sqrt{\pi}}{4} \right)^{2/3} T_e, \tag{58}$$

which agrees with the critical energy given in Ref. [7] ($Z_i = 1$ is assumed in Ref. [7]).]

Recall that $F^{f/e} \propto v_f$ while $F^{f/i} \propto 1/v_f^2$. Thus, if $v_f > v_{\text{crit}}$, then the collision friction of the beam ions with the background electrons will exceed the friction with the background ions.

5.1.4 Ratio between electron friction and ion friction

Using Eqs. (40) and (44), i.e.,

$$F^{f/e} = -4\Gamma^{f/e} \frac{1}{\sqrt{\pi}} \frac{1}{v_{te}^3} \frac{m_f}{m_e} \frac{v}{3}, \tag{59}$$

$$\sum_i F^{f/i} = -\frac{m_f}{v^2} \sum_i \frac{\Gamma^{f/i}}{m_i}, \tag{60}$$

and noting that $\Gamma^{a/b} = \frac{n_b q_a^2 q_b^2}{4\pi\epsilon_0^2 m_a^2} \ln\Lambda^{a/b}$ and $\ln\Lambda^{f/i} \approx \ln\Lambda^{f/e}$, the ratio between the two frictions is written as

$$\frac{\sum_i F^{f/i}}{F^{f/e}} = \frac{-\frac{m_f}{v^2} \sum_i \frac{\Gamma^{f/i}}{m_i}}{-4\Gamma^{f/e} \frac{1}{\sqrt{\pi}} \frac{1}{v_{te}^3} \frac{m_f}{m_e} \frac{v}{3}} = \frac{-\frac{m_f}{v^2} \sum_i \frac{n_i Z_i^2}{m_i n_e}}{-4 \frac{1}{\sqrt{\pi}} \frac{1}{v_{te}^3} \frac{m_f}{m_e} \frac{v}{3}} = \frac{3\sqrt{\pi}}{4} \frac{\frac{m_e}{v^3} \sum_i \frac{n_i Z_i^2}{m_i n_e}}{\frac{1}{v_{te}^3}}. \tag{61}$$

Using expression (51) of the critical velocity, the above expression is written as

$$\frac{\sum_i F^{f/i}}{F^{f/e}} = \frac{v_c^3}{v^3}. \tag{62}$$

which also shows that the electron friction is larger than ion friction when the fast ion veloicty v is larger than the critical veloicty v_c.

Similarly, $\nu_s^{(ai)}/\nu_s^{(e)}$ is written as

$$\frac{\nu_s^{(\text{ai})}}{\nu_s^{(e)}} = \frac{v_c^3}{v^3}. \tag{63}$$

5.1.5 Analytical solution to the slowing-down process

The $1/\nu_s$ is just a characteristic slowing-down time. A more accurate slowing-down time for a particle can be determined from the following differential equation:

$$\frac{dv}{dt} = F^{f/e} + \sum_i F^{f/i}, \tag{64}$$

Using $F^{f/e} = -v/t_s^{(e)}$, $\sum_i F^{f/i} = F^{f/e}(v_c/v)^3$, and $E = m v^2/2$, Eq. (64) is written as

$$\frac{dE}{dt} = -\frac{2}{t_e^{(s)}} E \left(1 + \left(\frac{E_c}{E} \right)^{3/2} \right) \tag{65}$$

which is Equation 5.4.10 in Wesson's book[9].

Assume that each energetic particle stay in the same magnetic surface where it is born (zero orbit-width approximation), then both $t_s^{(e)}$ and E_c are time constants during the slowing down process. Then equation (65) happens to have a closed form solution, thanks to that it is separable in variables:

$$-\frac{dE}{E\left(1+\left(\frac{E_c}{E}\right)^{3/2}\right)} = \frac{2}{t_e^{(s)}}dt. \tag{66}$$

The indefinite integration of the left-hand side is (I used `maxima` in finding this):

$$\ln\left(\frac{E_c}{E}\right) - \frac{2}{3}\ln\left[1+\left(\frac{E_c}{E}\right)^{3/2}\right]. \tag{67}$$

Then the solution to Eq. (66) is given by

$$\ln\left(\frac{E_c}{E}\right) - \frac{2}{3}\ln\left[1+\left(\frac{E_c}{E}\right)^{3/2}\right] = \frac{2}{t_e^{(s)}}t + C_0, \tag{68}$$

where C_0 is the integration constant. Equation (68) can be organized as

$$\ln\left\{\frac{E_c}{E}\left[1+\left(\frac{E_c}{E}\right)^{3/2}\right]^{(-2/3)}\right\} = \frac{2}{t_e^{(s)}}t + C_0, \tag{69}$$

i.e.,

$$\frac{E_c}{E}\left[1+\left(\frac{E_c}{E}\right)^{3/2}\right]^{(-2/3)} = C_1\exp\left(\frac{2}{t_e^{(s)}}t\right), \tag{70}$$

i.e.,

$$\left[\left(\frac{E_c}{E}\right)^{(-3/2)}+1\right]^{(-2/3)} = C_1\exp\left(\frac{2}{t_e^{(s)}}t\right), \tag{71}$$

i.e.,

$$\left(\frac{E}{E_c}\right)^{(3/2)}+1 = C_2\exp\left(-3\frac{t}{t_e^{(s)}}\right), \tag{72}$$

i.e.,

$$E = E_c\left[C_2 e^{-3t/t_e^{(s)}} - 1\right]^{2/3}. \tag{73}$$

At $t=0$, the above solution is written as

$$E(t=0) \equiv E_0 = E_c[C_2-1]^{2/3}. \tag{74}$$

from which we obtain

$$C_2 = 1 + \left(\frac{E_0}{E_c}\right)^{3/2} \tag{75}$$

In terms of E_0, Eq. (73) is written as

$$E = E_c\left[\left(1+\left(\frac{E_0}{E_c}\right)^{3/2}\right)e^{-3t/t_e^{(s)}} - 1\right]^{2/3}. \tag{76}$$

$$E = E_0\left[\left(\frac{E_c}{E_0}\right)^{3/2}\left(1+\left(\frac{E_0}{E_c}\right)^{3/2}\right)e^{-3t/t_e^{(s)}} - \left(\frac{E_c}{E_0}\right)^{3/2}\right]^{2/3}. \tag{77}$$

$$E = E_0\left[\left(\left(\frac{E_c}{E_0}\right)^{3/2} + 1\right)e^{-3t/t_e^{(s)}} - \left(\frac{E_c}{E_0}\right)^{3/2}\right]^{2/3}. \tag{78}$$

$$E = E_0\left[e^{-3t/t_e^{(s)}} - \left(\frac{E_c}{E_0}\right)^{3/2}\left(1 - e^{-3t/t_e^{(s)}}\right)\right]^{2/3}, \tag{79}$$

Equation (79) agrees with Eq. (5.4.11) in Ref. [9]. From the solution in Eq. (79), the time needed for a particle of energy E_0 to slow down to a cutoff energy E can be calculated. Equation (79) can be re-organized as

$$\left(\frac{E}{E_0}\right)^{3/2} = e^{-3t/t_e^{(s)}} - \left(\frac{E_c}{E_0}\right)^{3/2}\left(1 - e^{-3t/t_e^{(s)}}\right). \tag{80}$$

i.e.,

$$\left[1 + \left(\frac{E_c}{E_0}\right)^{3/2}\right]e^{-3t/t_e^{(s)}} = \left(\frac{E_c}{E_0}\right)^{3/2} + \left(\frac{E}{E_0}\right)^{3/2} \tag{81}$$

i.e.,

$$t = \frac{t_e^{(s)}}{3}\ln\left[\frac{1 + \left(\frac{E_c}{E_0}\right)^{3/2}}{\left(\frac{E}{E_0}\right)^{3/2} + \left(\frac{E_c}{E_0}\right)^{3/2}}\right], \tag{82}$$

which gives the time it takes for a particle of energy E_0 to slow down to a cutoff energy E. When the cutoff energy is zero, the above time is written as

$$t = \frac{t_e^{(s)}}{3}\ln\left[\frac{1 + \left(\frac{E_c}{E_0}\right)^{3/2}}{\left(\frac{E_c}{E_0}\right)^{3/2}}\right], \tag{83}$$

i.e.,

$$t = \frac{t_e^{(s)}}{3}\ln\left[1 + \left(\frac{E_0}{E_c}\right)^{3/2}\right] \equiv t_s. \tag{84}$$

We call this time span the slowing-down time.

5.2 Steady-state energetic particle density and pressure

The steady-state density of fast ions at a radial location is given by

$$\begin{aligned}
n_\alpha(\psi) &= \int_0^{t_s} F_{\text{source}}(\psi)dt \\
&= F_{\text{source}}(\psi)\int_0^{t_s} dt \\
&= F_{\text{source}}(\psi)t_s \\
&= F_{\text{source}}(\psi)\frac{t_e^{(s)}}{3}\ln\left[1 + \left(\frac{E_0}{E_c}\right)^{3/2}\right].
\end{aligned} \tag{85}$$

where, for α particles, $F_{\text{source}} = n_D n_T \langle \sigma v \rangle$ is the fusion rate $(m^{-3}s^{-1})$, while, for NBI, F_{source} can be obtained from the MC deposition module.

Similary, the steady-state kinetic energy density K_α at a radial location is given by

$$K_\alpha = \int_0^{t_s} E(t) F_{\text{source}} dt = F_{\text{source}} \int_0^{t_s} E(t) dt, \tag{86}$$

Using $E(t)$ given by Eq. (79), the above time integration can be numerically evaluated. The integration can also be analytically evaluated. Using Eq. (79), the time integration is written as

$$\int_0^{t_s} E(t) dt = \int_0^{t_s} E_0 \left[e^{-3t/t_e^{(s)}} - \left(\frac{E_c}{E_0} \right)^{3/2} \left(1 - e^{-3t/t_e^{(s)}} \right) \right]^{2/3} dt. \tag{87}$$

Define $y \equiv E_0 / E_c$, $\tau_s \equiv t_s / t_e^{(e)} = \frac{1}{3}\ln(1 + y^{3/2})$, and $\tau \equiv t / t_e^{(s)}$, then expression (87) is written as

$$\int_0^{t_s} E(t) dt = E_0 t_e^{(s)} \int_0^{\tau_s} [e^{-3\tau} - y^{-3/2}(1 - e^{-3\tau})]^{2/3} d\tau$$

Let us use `maxima` to perform the above definite integral:

```
Maxima 5.43.2 http://maxima.sourceforge.net
using Lisp GNU Common Lisp (GCL) GCL 2.6.12
Distributed under the GNU Public License. See the file COPYING.
Dedicated to the memory of William Schelter.
The function bug_report() provides bug reporting information.
```

(%i1) `assume(y>0);`

(%o1) $[y > 0]$

(%i3) `integrate((exp(-3*tao)- y**(-3/2)*(1-exp(-3*tao)))**(2/3),`
`tao, 0,log(1+y**(3/2))/3);`

(%o3) $-\dfrac{\log\left(\dfrac{\left|y^2 - y^{\frac{3}{2}} + y\right|}{y}\right)}{6y} - \dfrac{\arctan\left(\dfrac{2\sqrt{3}\sqrt{y} - \sqrt{3}}{3}\right)}{\sqrt{3}\,y} + \dfrac{\log(\sqrt{y} + 1)}{3y} - \dfrac{\pi}{2\,3^{\frac{3}{2}}\,y} + \dfrac{1}{2}$

(%i4)

The result can be simplified as (noting that $\arctan(1/\sqrt{3}) = \pi/6$):

$$-\frac{\log\left(\frac{|y - \sqrt{y} + 1|}{(\sqrt{y} + 1)^2}\right)}{6y} - \frac{\arctan\left(\frac{2\sqrt{y} - 1}{\sqrt{3}}\right)}{\sqrt{3}\,y} - \frac{\arctan(1/\sqrt{3})}{\sqrt{3}\,y} + \frac{1}{2}, \tag{88}$$

which agrees with Eq. 5.B-9 in the ONETWO manual[6]. Then K_α is written as

$$
\begin{aligned}
K_\alpha \;=\;& F_{\text{source}} E_0 t_e^{(s)} \left[-\frac{1}{6\,y} \log\left(\frac{|y - \sqrt{y} + 1|}{(\sqrt{y}+1)^2} \right) \right. \\
& \left. - \frac{\arctan\left(\frac{2\sqrt{y}-1}{\sqrt{3}} \right)}{\sqrt{3}\,y} - \frac{\arctan(1/\sqrt{3})}{\sqrt{3}\,y} + \frac{1}{2} \right],
\end{aligned}
\tag{89}
$$

where log is the natural logarithm. Note that F_{fusion}, $t_e^{(s)}$ and E_c (and thus y) depends on the radial location.

The pressure is then given by

$$
P_\alpha = \frac{2}{3} K_\alpha.
\tag{90}
$$

5.3 Steady-state heating power density (delivered to ions and electrons) from energetic α particles

The steady-state heating power density (delivered to background plasma) from α particles is given by

$$
\begin{aligned}
H \;=\;& \int_0^{t_s} \left(-\frac{dE}{dt} \right) F_{\text{source}}(\psi)\,dt. \\
=\;& -F_{\text{source}}(\psi) \int_0^{t_s} dE \\
=\;& F_{\text{source}}(\psi) E_0.
\end{aligned}
\tag{91}
$$

The slowing-down equation (65) can be split into two parts (electron/ion contribution):

$$
\left(\frac{dE}{dt} \right)_e = -\frac{2}{t_e^{(s)}} E
\tag{92}
$$

$$
\left(\frac{dE}{dt} \right)_i = -\frac{2}{t_e^{(s)}} E \left(\frac{E_c}{E} \right)^{3/2}
\tag{93}
$$

Then, the steady-state heating power density delivered to background electrons is written as

$$
\begin{aligned}
H_e \;=\;& \int_0^{t_s} \left[-\left(\frac{dE}{dt} \right)_e \right] F_{\text{source}}(\psi)\,dt. \\
=\;& F_{\text{source}}(\psi) \frac{2}{t_e^{(s)}} \int_0^{t_s} E(t)\,dt
\end{aligned}
\tag{94}
$$

$$
= K_\alpha \frac{2}{t_e^{(s)}}.
\tag{95}
$$

Similarly, the steady-state heating power density delivered to background ions is written as

$$
\begin{aligned}
H_i &= \int_0^{t_s}\left[-\left(\frac{dE}{dt}\right)_i\right]F_{\text{source}}(\psi)dt. \\
&= F_{\text{source}}(\psi)\frac{2}{t_e^{(s)}}E_c^{3/2}\int_0^{t_s}\frac{1}{\sqrt{E}}dt,
\end{aligned}
\tag{96}
$$

Here we note that the integrand is singular at $E(t = t_s) = 0$. To avoid this difficulty, we can choose a cutoff energy which is not eactly zero (as we do in the simulation). We can also calculate H_i by $H_i = H - H_e$, which avoids direct calculation of the above integration.

For α particles, there is a single brith energy, $E_0 \approx 3.52\text{MeV}$. For NBI, typically there are three initial kinetic energies: full, half, one third. The above formulas can be applied to each energy, and then we sum the results to get the total heating. For NBI, in code implementation, the source term $F_{\text{source}}(\psi, E_0)$ is not actually used. Instead, MC deposition is used for each marker, with their weight, energy, radial position taken into account.

5.4 Monte-Carlo algorithm of fast ion collisions with background plasma

The pitch $\lambda = v_\parallel / v$ and velocity v of fast ions are altered at the end of each time step according to the following Monte-Carlo algorithm (Refer to Todo's paper [8]):

$$
\lambda_{\text{new}} = \lambda(1 - \nu_d\Delta t) \pm \sqrt{(1 - \lambda^2)\nu_d\Delta t},
\tag{97}
$$

and

$$
\begin{aligned}
v_{\text{new}} &= v - \nu_s^{(e)}\Delta t\, v\left(1 + \frac{v_c^3}{v^3}\right) \\
&+ \frac{\nu_s^{(e)}\Delta t}{m_f v}\left[T_e - \frac{1}{2}T_i\left(\frac{v_c}{v}\right)^3\right] \pm \sqrt{\frac{\nu_s^{(e)}\Delta t}{m_f}\left[T_e + T_i\left(\frac{v_c}{v}\right)^3\right]},
\end{aligned}
\tag{98}
$$

where Δt is the time step, $\nu_s^{(e)}$ is the slowing down (due to electrons) rate given by Eq. (47), ν_d is the pitch-angle scattering rate given by

$$
\nu_d = Z_{\text{eff}}\nu_0 = Z_{\text{eff}}\frac{\Gamma^{f/e}}{v^3} = \left(\frac{Z_{\text{eff}}}{v^3}\right)\frac{n_e Z_f^2 e^4 \ln\Lambda^{\alpha/e}}{4\pi\varepsilon_0^2 m_f^2},
\tag{99}
$$

where Z_f is the charge number of fast ions, Z_{eff} is the effective charge number of background ions,

$$
Z_{\text{eff}} \approx \sum_i \frac{n_i Z_i^2}{n_e}.
\tag{100}
$$

The blue term corresponds to the energy diffusion and $\pm$ denotes a randomly chosen sign with equal probability for plus and minus.

Note that the pitch-angle scattering is solely due to ions, while slowing-down and energy diffusion are due to both ions and electrons.

5.5 Heating power

The heating power (from fast ions) to bulk plasma within a given spatial volume V is equal to the fast ion kinetic energy loss rate within that volume, i.e.,

$$P = \sum_{j=1}^{N} w_j \frac{\Delta E_j}{\Delta t}, \tag{101}$$

where N is the number of markers within the given spatial volume V, w_j is the marker weight, ΔE_j is the kinetic energy decrease of a marker duing the time interval Δt. Using $\Delta E_j = \frac{1}{2}mv_{j,\text{old}}^2 - \frac{1}{2}mv_{j,\text{new}}^2$, expression (101) is written as

$$P = \sum_{j=1}^{N} w_j \frac{\frac{1}{2}mv_{j,\text{old}}^2 - \frac{1}{2}mv_{j,\text{new}}^2}{\Delta t}. \tag{102}$$

Using the algorithm of Eq. (98) and keeping only the slowing-down term (i.e., neglecting the energy diffusion), i.e.,

$$v_{j,\text{new}} = v_{j,\text{old}} - v_{j,\text{old}} \nu_s^{(e)} \Delta t (C_i + C_e), \tag{103}$$

where $C_i = \left(\frac{v_c}{v_{j,\text{old}}}\right)^3, C_e = 1$, expression (102) is written as

$$
\begin{aligned}
P &= \frac{1}{2}\frac{m}{\Delta t}\sum_{j=1}^{N} w_j \left\{ v_{j,\text{old}}^2 - \left[v_{j,\text{old}} - v_{j,\text{old}} \nu_s^{(e)} \Delta t (C_i + C_e) \right]^2 \right\}, \\
&= \frac{1}{2}m\sum_{j=1}^{N} w_j \left\{ -v_{j,\text{old}}^2 \nu_s^{(e)} (C_i + C_e)^2 \nu_s^{(e)} \Delta t + 2v_{j,\text{old}}^2 \nu_s^{(e)}(C_i + C_e) \right\} \qquad (104)
\end{aligned}
$$

Neglecting the first term (which is smaller than the second term by a factor of $\nu_s \Delta t \ll 1$), expression (104) is written as

$$
\begin{aligned}
P &\approx \frac{1}{2}m\sum_{j=1}^{N} w_j \left[2v_{j,\text{old}}^2 \nu_s^{(e)}(C_i + C_e) \right] \\
&= P_i + P_e, \tag{105}
\end{aligned}
$$

where

$$P_i = m\sum_{j=1}^{N} w_j v_{j,\text{old}}^2 \nu_s^{(e)} C_i, \tag{106}$$

and

$$P_e = m\sum_{j=1}^{N} w_j v_{j,\text{old}}^2 \nu_s^{(e)} C_e, \tag{107}$$

are the heating power delivered to the thermal ions and electrons, respectively.

The heating power density is given by

$$\frac{P}{V} \tag{108}$$

5.6 NBI collisional torque

The toroidal force to bulk plasma (due to fast ion colliding on bulk plasma) within a given spatial volume is equal to the fast ion toroidal momentum loss rate within that volume, i.e.,

$$F_\phi \approx m_f \sum_{j=1}^{N} w_j \frac{\Delta v_{\phi j}}{\Delta t}, \tag{109}$$

where the summation is over the markers that are within the volume, $\Delta v_{\phi j} \equiv v_{\phi j}^{(old)} - v_{\phi j}^{(new)}$ is the toroidal velocity descrease of the jth marker in the time interval Δt due to collision. The corresponding torque is then given by

$$T_\phi = m_f \sum_{j=1}^{N} w_j \frac{\Delta v_{\phi j}}{\Delta t} R_j, \tag{110}$$

where R_j is the cylindrical coordinate R of the jth marker. For simplicity, v_ϕ is approximated by $v_\parallel$ or $-v_\parallel$ (depending on the sign of B_ϕ) in numerical implementation.

Coulomb logarithm for electron-ion collisions is given in Page. 34 of NRL2018version:

$$\ln\Lambda = 24 - \ln\left(n_e^{1/2} T_e^{-1}\right) \tag{111}$$

where n_e, T_e are in units of cm^{-3} and eV, respectively. Then

$$
\begin{aligned}
\ln\Lambda &= 24 - \ln\left(n_e^{1/2}\right) - \ln(T_e^{-1}) \\
&= 24 - \frac{1}{2}\ln(n_e) + \ln(T_e) \\
&= 24 - \frac{1}{2}\ln\left(\frac{n_{e0}}{10^6}\right) + \ln(10^3 T_{e0}) \\
&= 24 - \frac{1}{2}\ln\left(\frac{n_{e0}}{10^{20}} 10^{14}\right) + \ln(10^3) + \ln(T_{e0}) \\
&= 24 - \frac{1}{2}\ln\left(\frac{n_{e0}}{10^{20}}\right) - \frac{1}{2}\ln(10^{14}) + \ln(10^3) + \ln(T_{e0}) \\
&= 14.79 - \frac{1}{2}\ln\left(\frac{n_{e0}}{10^{20}}\right) + \ln(T_{e0})
\end{aligned}
\tag{112}
$$

where n_{e0}, T_{e0} are in units of m^{-3} and keV, respectively.

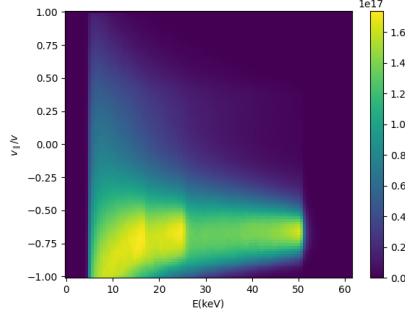For BEST tokamak, $\ln\Lambda \approx 17$.

Figure 43. Steady-state distribution of fast ions in $(E, v_\parallel/v)$ space.

5.7 Current driven by beam

5.8 Monte-Carlo implementation given in Z. Lin's paper[5], not verified

Z. Lin's paper[5] provided a Monte-Carlo method of implementing the collision of a test particle with a Maxwellian background species, which is given by (how to derive these formula from a known collision operator?)

$$v_\parallel = v_{\parallel 0} - \nu_{s\parallel}\Delta t + \sqrt{12}(R_1 - 0.5)\sqrt{\nu_\parallel \Delta t}, \tag{113}$$

and

$$v_\perp^2 = v_{\perp 0}^2 - \nu_{s\perp}\Delta t + \sqrt{12}(R_2 - 0.5)\sqrt{\left(\nu_\perp - \frac{\nu_{\parallel\perp}^2}{\nu_\parallel}\right)\Delta t} + \sqrt{12}(R_1 -$$

$$0.5)\frac{\nu_{\parallel\perp}}{\nu_\parallel}\sqrt{\nu_\parallel \Delta t} \tag{114}$$

where R_1 and R_2 are two independent random numbers chosen from a uniform distribution from 0 to 1, Δt is the time step, $\nu_{s\parallel}, \nu_{s\perp}, \nu_\parallel, \nu_\perp$, and $\nu_{\parallel\perp}$ are given by

$$\nu_{s\parallel} = v_\parallel\left(1 + \frac{m_\alpha}{m_\beta}\right)F\nu_0, \tag{115}$$

$$\nu_{s\perp} = \left[2v_\perp^2\left(1 + \frac{m_\alpha}{m_\beta}\right)F - v_\perp^2 H - (2v_\parallel^2 + v_\perp^2)G\right]\nu_0, \tag{116}$$

$$\nu_\parallel = [v_\parallel^2 H + v_\perp^2 G]\nu_0, \tag{117}$$

$$\nu_\perp = [4v_\perp^2(v_\perp^2 H + v_\parallel^2 G)]\nu_0 \tag{118}$$

$$\nu_{\parallel\perp} = [2v_\perp^2 v_\parallel(H - G)]\nu_0, \tag{119}$$

with F, G, and H defined by

$$F = \phi(x), \tag{120}$$

$$G = \left(1 - \frac{1}{2x}\right)\phi(x) + \frac{d\phi(x)}{dx}, \tag{121}$$

$$H = \frac{1}{x}\phi(x), \tag{122}$$

where $x = v^2/v_{\text{th}\beta}^2$ and $\phi(x)$ is the Maxwellian integral defined by

$$\phi(x) = \frac{2}{\sqrt{\pi}}\int_0^x e^{-t}\sqrt{t}\,dt,$$

which can be written in terms of the error function as (using `maxima`)

$$\phi(x) = \frac{e^{-x}}{\sqrt{\pi}}\left[\sqrt{\pi}\,\text{erf}(\sqrt{x})e^x - 2\sqrt{x}\right]. \tag{123}$$

The basic collision frequency ν_0 is defined by

$$\nu_0 = \frac{\Gamma^{\alpha/\beta}}{v^3} = \frac{n_\beta q_\alpha^2 q_\beta^2 \ln\Lambda^{\alpha/\beta}}{4\pi\varepsilon_0^2 m_\alpha^2 v^3}, \tag{124}$$

(This formula is different from the formula given in Lin's paper[5], it seems that Lin misused a formula of Gauss-unit in the paper that uses S.I units elsewhere).

The above formula can be applied to model collisions of fast particles with both ions and electrons.

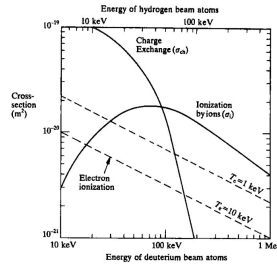## A   Ionization cross section given in Wesson's book

Figure 44. Fig. 5.3.1 of Wesson's book "Tokamaks", which shows the cross-sections for charge exchange and ionization by plasma ions and the effective cross-section for ionization by electrons, as functions of the energy of neutral beam atoms.

A.1 Continuous beam injection

To obtain the steady state of fast ions on the long slowing-down time scale, we need take into account the continuous beam source. A straightforward Monte-Carlo implementation of this continuous injection is to introduce new Monte-Carlo markers to represent the newly injected physical particles at each time step. This method is computationally expensive. For a time-independent background plasma, there is an efficient method that involves only a single injection and then utilizes the time shift invariance to infer the contribution of all the other injections. This method is illustrated in Fig. 45.
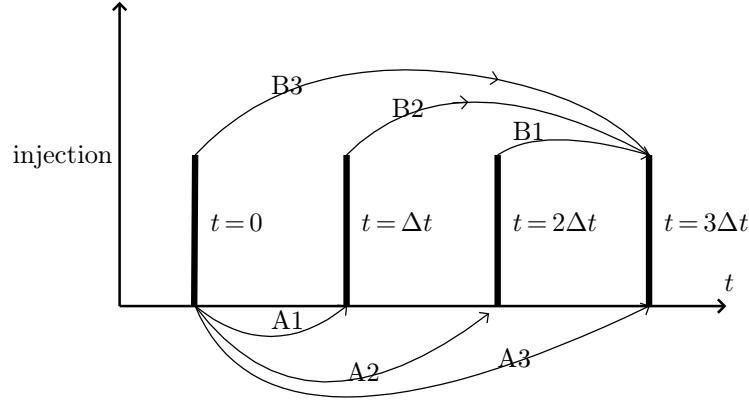

Figure 45. An efficient way of simulating multiple injections. The contribution of injections at $t = j\Delta t$ with $j = 0, 1, 2$ to the fast ion distribution at $t = 3\Delta t$ can be obtained by following the time history of the particles injected at $t = 0$ and recording their contribution to the fast ion distribution at $t = \Delta t, 2\Delta t, 3\Delta t$, indicated respectively by $A1$, $A2$, and $A3$. Then it is ready to see that $B1 = A1$, $B2 = A2$, and $B3 = A3$. Therefore the contributions of the multiply injections can be inferred from the time history of a single injection.

The above method works only for a time-independent background plasma and constant beam power. For time-dependent background plasma or beam power, re-injecting new Monte-Carlo markers seems to be the only solution. This work will consider a time-independent background plasma with a constant beam power and use the above efficient method.

Bibliography

[1]   O. Demokan and V. Mirnov. Rigorous treatment of charge exchange, ionization, and collisional processes in neutral-beam-injected mirrors. *Physics of Plasmas*, 2(1):139–145, 1995.

[2] R. K. Janev and J. J. Smith. Cross sections for collision processes of hydrogen atoms with electrons, protons and multiply charged ions. *Atomic and Plasma-material Interaction Data for Fusion*, 4, 1993.

[3] Igor D. Kaganovich, Edward A. Startsev, and Ronald C. Davidson. Scaling cross sections for ion-atom impact ionization. *Physics of Plasmas*, 11(3):1229–1232, 2004.

[4] Charles F. F. Karney. Fokker-planck and quasilinear codes. *Comp. Phys. Rep.*, 4:183–244, 1986.

[5] Z. Lin, W. M. Tang, and W. W. Lee. Gyrokinetic particle simulation of neoclassical transport. *Physics of Plasmas*, 2(8):2975, 1995.

[6] W. W. Pfeiffer, R. H. Davidson, R. L. Miller, and R. E. Waltz. Onetwo: a computer code for modeling plasma transport in tokamaks. Technical Report, General Atomics, San Diego, CA (United States), 12 1980.

[7] ITER physics basis editors. Chapter 5: physics of energetic ions. *Nucl. Fusion*, 39(12):2471, 1999.

[8] Y. Todo, M.A. Van Zeeland, A. Bierwage, and W.W. Heidbrink. Multi-phase simulation of fast ion profile flattening due to alfvén eigenmodes in a diii-d experiment. *Nucl. Fusion*, 54(10):104012, 2014.

[9] John Wesson. *Tokamaks*. Oxford University Press, 2004.